Draft version November 4, 2025
Typeset using LaTeX **twocolumn** style in AASTeX7.0.1

A Test of Substellar Evolutionary Models with High-Precision Ages from Asteroseismology and Gyrochronology for the Benchmark System HR 7672AB

Yaguang Li (李亚光) [1] Michael C. Liu [1] Trent J. Dupuy [2] Daniel Huber [1] Jingwen Zhang (张婧雯) [1,3] Daniel Hey [1] R.R. Costa [4,5] Jens Reersted Larsen [6] J. M. Joel Ong (王加冕) [1,*] Sarbani Basu [7] Travis S. Metcalfe [8] Yixiao Zhou (周一啸) [9] Jennifer van Saders [1] Timothy R. Bedding [10] Marc Hon [11] Hans Kjeldsen [6] Tiago L. Campante [4,5] Mário J. P. F. G. Monteiro [4,5] Mia Sloth Lundkvist [6] Mark Lykke Winther [6] Ashley Chontos [12] Nicholas Saunders [1,†] Theron W. Carmichael [1] Antonin Bouchez [13] Carlos Alvarez [13] Aldo G. Sepulveda [1] Howard Isaacson [14] Andrew W. Howard [15] Steven R. Gibson [16] Samuel Halverson [17] Kodi Rider [18] Arpita Roy [19] Ashley D. Baker [16] Jerry Edelstein [18] Chris Smith [18] Benjamin J. Fulton [20] and Josh Walawender [13]

[1] *Institute for Astronomy, University of Hawai'i, 2680 Woodlawn Drive, Honolulu, HI 96822, USA*
[2] *Institute for Astronomy, University of Edinburgh, Royal Observatory, Blackford Hill, Edinburgh EH9 3HJ, UK*
[3] *Department of Physics, University of California, Santa Barbara, CA 93106, USA*
[4] *Instituto de Astrofísica e Ciências do Espaço, Universidade do Porto, Rua das Estrelas, 4150-762 Porto, Portugal*
[5] *Departamento de Física e Astronomia, Faculdade de Ciências da Universidade do Porto, Rua do Campo Alegre, s/n, 4169-007 Porto, Portugal*
[6] *Stellar Astrophysics Centre (SAC), Department of Physics and Astronomy, Aarhus University, Ny Munkegade 120, 8000 Aarhus C, Denmark*
[7] *Department of Astronomy, Yale University, New Haven, CT 06511, USA*
[8] *Center for Solar-Stellar Connections, WDRC, 9020 Brumm Trail, Golden, CO 80403, USA*
[9] *Rosseland Centre for Solar Physics, University of Oslo, PO Box 1029 Blindern, 0315 Oslo, Norway*
[10] *Sydney Institute for Astronomy (SIfA), School of Physics, University of Sydney, NSW 2006, Australia*
[11] *Department of Physics, National University of Singapore, 21 Lower Kent Ridge Road, 119077, Singapore*
[12] *Department of Astrophysical Sciences, Princeton University, 4 Ivy Lane, Princeton, NJ 08540, USA*
[13] *W. M. Keck Observatory, 65-1120 Mamalahoa Hwy, Kamuela, HI 96743, USA*
[14] *Department of Astronomy, 501 Campbell Hall, University of California, Berkeley, CA 94720, USA*
[15] *Department of Astronomy, California Institute of Technology, Pasadena, CA 91125, USA*
[16] *Caltech Optical Observatories, California Institute of Technology, Pasadena, CA 91125, USA*
[17] *Jet Propulsion Laboratory, California Institute of Technology, 4800 Oak Grove Drive, Pasadena, CA 91109, USA*
[18] *Space Sciences Laboratory, University of California, Berkeley, CA 94720, USA*
[19] *Astrophysics & Space Institute, Schmidt Sciences, New York, NY 10011, USA*
[20] *NASA Exoplanet Science Institute/Caltech-IPAC, California Institute of Technology, Pasadena, CA 91125, USA*

ABSTRACT

We present high-precision measurements for HR 7672AB, composed of a Sun-like (G0V) star and an L dwarf companion. Three nights of precise (70 cm/s) radial velocity (RV) asteroseismology with the Keck Planet Finder clearly detect 5-minute oscillations from the primary HR 7672A, and modeling of the frequency spectrum yields an asteroseismic age of 1.87 ± 0.65 Gyr. We also determine a gyrochronological age of 2.58 ± 0.47 Gyr from the primary's chromospheric activity, and we combine these two results for a final age of 2.26 ± 0.40 Gyr. In addition, we obtained new imaging for the companion HR 7672B, thereby refining dynamical mass to 75.39 ± 0.67 M_{Jup}, which places it near the stellar/substellar boundary and thus particularly sensitive to differences in model predictions. The joint precision in host star age (18% uncertainty) and companion mass (0.9% uncertainty) makes HR 7672AB an exceptional substellar benchmark. Combined with the companion's luminosity, we use these measurement to test predictions from six brown dwarf cooling models. The best agreement occurs with the Chabrier et al. (2023) models, which incorporate a new equation of state, resulting in predictions that agree within $<0.3\sigma$ with all the observations. The other 5 sets of models agree at the 1–3σ level depending on the particular test, and some models struggle to predict a sufficient low luminosity for HR 7672B at any age given its dynamical mass. Finally, we detected a weak seismic signal in near-simultaneous TESS photometry of HR 7672A, with the resulting RV-to-photometry oscillation amplitude ratio consistent with solar values.

Email: yaguangl@hawaii.edu

Keywords: Late-type dwarf stars (906), L dwarfs (894), Asteroseismology (73), Stellar radii (1626), Stellar masses (1614), Stellar rotation (1629), Radial velocity (1332), Astrometry (80), Stellar magnetic fields (1610), Stellar evolutionary models (2046), Brown dwarfs (185), Stellar activity (1580), High resolution spectroscopy (2096)

1. INTRODUCTION

Brown dwarfs are objects with masses between the heaviest gas-giant planets and the lowest-mass stars (≈13–75 M_{Jup}; e.g., G. Chabrier & I. Baraffe 2000; T. J. Dupuy & M. C. Liu 2017). They are not massive enough to sustain stable hydrogen fusion, which is the process that powers main-sequence stars. Instead, brown dwarfs can briefly fuse deuterium, and those above ~65 M_{Jup} can fuse lithium early in their evolution. Without a long-lived fusion source, brown dwarfs cool and fade as they radiate away their residual heat. Their effective temperature and luminosity steadily decrease with age, causing them to evolve through later spectral types (from late-M to L to T and Y). This contrasts with main-sequence stars, which maintain stable luminosities for millions to trillions of years.

The cooling of brown dwarfs is predicted by evolutionary models. Early models used simplified treatments of interior and atmospheric physics, but the low temperatures of brown dwarfs require more sophisticated approaches. Modern models incorporate non-grey atmospheres (e.g., A. Burrows et al. 1997; G. Chabrier & I. Baraffe 1997; M. S. Marley et al. 2021), dust and cloud physics (e.g., G. Chabrier & I. Baraffe 2000; I. Baraffe et al. 2002; D. Saumon & M. S. Marley 2008; C. V. Morley et al. 2012), disequilibrium chemistry (e.g., D. Saumon et al. 2006; M. W. Phillips et al. 2020a), vertical mixing (e.g., P. Tremblin et al. 2015), detailed equations of state and degeneracy (e.g., G. Chabrier et al. 2023), and assumptions about initial conditions (e.g. hot vs. cold start; e.g., M. S. Marley et al. 2007).

Evolutionary models provide predictions of brown dwarf luminosity, radius, and effective temperature at a given age and mass, often visualized as cooling curves (luminosity vs. age at fixed masses) and isochrones (radius vs. mass at fixed ages). When coupled to model atmospheres, such models also predict the mass- and age-dependence of an object's colors, magnitudes, and spectra. Thus, evolutionary models are at the heart of converting observations into the fundamental properties needed to understand both individual objects and the substellar population as a whole.

Given the wide-spread use of such models, testing their predictions is imperative. To do so, model-independent measurements of brown dwarf properties are needed, in particular the 3 key quantities of luminosity, age, and mass. Systems with at least 2 of these quantities measured are often referred to as "benchmarks" (e.g. M. C. Liu et al. 2008). While luminosities is relatively easy to measure, age and mass are not for most brown dwarfs, which are free-floating objects. For a minority fraction of known objects, ages can be established via their physical association with a star or stellar association (e.g. D. J. Pinfield et al. 2006). And for an even smaller fraction of the known objects, dynamical masses can be measured via the visual/astrometric orbits of binary brown dwarfs (e.g., T. J. Dupuy & M. C. Liu 2017) and brown dwarfs that are companions to nearby stars (e.g. T. D. Brandt et al. 2019).

Only a tiny fraction of known brown dwarfs have their luminosities, ages, and masses all measured. Such systems provide the most stringent tests of evolutionary models. For instance, using the models with the observed dynamical mass and luminosity produces a "cooling age" for the brown dwarf, which can be compared with the primary star's age. This test was first done by T. J. Dupuy et al. (2009), who found that the cooling age for the brown dwarf binary HD 130948BC (440±40 Myr) was inconsistent with the age of the solar-type host star HD 130948A as inferred from gyrochronology (790±150 Myr). Or put another way, the brown dwarfs appear to be 2–3× overluminous compared to model predictions given their masses and age. Evidence for a discrepancy between cooling ages and stellar ages has steadily grown in recent years, with now a ≈half a dozen star+brown dwarf systems where the brown dwarf potentially shows either over- or under-luminosity relative to evolutionary model predictions (e.g., G. M. Brandt et al. 2021 and references therein). However, the discrepancy between model predictions and observation shown no clear pattern of behavior, limiting our ability to probe for the origin. One key limiting factor is that the measured ages for these benchmarks are often imprecise.

This paper focuses on one notable benchmark system, HR 7672AB, composed of a Sun-like (G0V) and an imaged L dwarf companion with a 17 au semi-major axis. Studying the primary star HR 7672A (15 Sge; HD 190406) provides two critical measurements for testing evolutionary models: (1) a dynamical mass measurement for the companion based on its orbit, and (2) a stellar age estimate that applies to the system as a whole, under the conservative assumption of both components being coeval.

HR 7672B was discovered by M. C. Liu et al. (2002) with adaptive optics (AO) imaging at Keck and Gemini and shed light on the "brown dwarf desert," namely the scarcity of ≈15–75M_{Jup} companions in radial velocity surveys of solar-type stars. At ≈14 AU (0.8") projected separation, HR 7672B demonstrated that brown dwarfs, while rare, can exist at planet-like separations. A decade later, J. R. Crepp et al. (2012) measured its orbit, finding a ≈73-year period, high eccentricity ($e \approx 0.5$), and near edge-on inclination, and continued orbital monitoring by B. P. Bowler et al. (2023) showed no signs of spin-orbit misalignment. Its eccentricity may re-

[*] NASA Hubble Fellow
[†] NSF Graduate Research Fellow

flect dynamical interactions (e.g., with a passing star or unseen companion) or simply the outcome of fragmentation-based formation, which naturally yields eccentric orbits (unlike the near-circular orbits typical of disk-formed planets).

More recently, HR 7672B's atmosphere has been studied with AO-assisted high-spectral resolution measurements. J. Wang et al. (2022) used K-band spectroscopy with Keck/KPIC to measure carbon and oxygen abundances, key to CO, H_2O, and CH_4 chemistry. The elemental abundances of the host star agree well with the host star, supporting a star-like formation scenario for the companion. Y. Kasagi et al. (2025) further obtained high-resolution YJH-band spectra with Subaru/REACH. Their atmospheric retrievals detected H_2O and FeH absorption and required an optically thick cloud layer to reproduce the data, consistent with L-dwarf cloud physics. They inferred cloud-top temperatures suggestive of condensates such as TiO_2, Al_2O_3, or Fe.

In this study, we derive the age of HR 7672A — and hence the system — using asteroseismology from three consecutive nights of Keck Planet Finder (KPF) radial velocity data and with gyrochronology based on stellar rotation (§2–§3). We also refine the dynamical mass of HR 7672B, using a new epoch of AO imaging combined with additional RV data for the primary. These new high-precision measurements of the system enable strong tests of current substellar evolutionary models (§4). We also discuss the nearly-simultaneous KPF and TESS observations, which offer additional insights into stellar pulsations (§5).

2. OBSERVATIONS

2.1. *Asteroseismology with Keck Planet Finder*

Asteroseismology is the study of stellar oscillations, which probe internal structure and provide precise fundamental stellar properties. Extremely Precise Radial Velocity (EPRV) techniques now achieve radial velocity measurements with precisions down to 30 cm/s for individual measurements (D. A. Fischer et al. 2016; J. T. Wright 2018). At this precision, stars that oscillate at very low amplitudes to be detected from photometry like TESS (G. R. Ricker et al. 2015), such as main-sequence K dwarfs, can now be routinely detected via the EPRV method. Oscillations have recently been detected in K-type main-sequence dwarfs with amplitudes of only 1–6 cm/s in ϵ Ind A (T. L. Campante et al. 2024; M. S. Lundkvist et al. 2024), σ Dra (M. Hon et al. 2024b) and HD 219134 (Y. Li et al. 2025), as well as in the subgiant HD 118203 (J. Zhang et al. 2024).

The advantage of the EPRV method is particularly great for young, magnetically active stars. Their oscillation amplitudes are, in general, smaller than those of older stars (D. Huber et al. 2011a; T. L. Campante et al. 2014; M. Sayeed et al. 2025), so their oscillations can often be obscured by granulation or white noise in photometry. EPRV is less sensitive to granulation at oscillation frequencies of interest, enabling higher SNR of oscillations in such targets. The star we are studying, HR 7672A, is a moderately young G-type dwarf that illustrates this capability.

Table 1. Oscillation frequencies of HR 7672, including corrections for line-of-sight Doppler shifts.

n	ℓ	$\nu_{n,\ell}$	$\sigma(\nu_{n,\ell})$
		μHz	μHz
18	0	2572.67	1.75
19	0	2703.14	1.74
20	0	2834.84	1.25
21	0	2965.31	1.66
22	0	3098.25	0.93
24	0	3366.58	1.26
25	0	3498.28	1.79
18	1	2631.75	1.62
19	1	2762.22	1.61
20	1	2895.16	1.35
21	1	3028.09	1.32
22	1	3159.79	0.74
23	1	3293.96	1.15
25	1	3559.82	0.84
19	2	2822.53	1.27
20	2	2954.24	0.59
21	2	3087.17	1.33
22	2	3220.10	0.84
23	2	3350.58	0.90
24	2	3487.20	1.39
25	2	3620.14	1.53
21	3	3141.33	1.40
22	3	3276.72	1.42

We obtained approximately 8 hours of observations per night over 3 consecutive nights, from July 12 to 14, 2024 (Hawaii Standard Time), using the Keck Planet Finder (KPF) mounted on the Keck I telescope (S. R. Gibson 2016; S. R. Gibson et al. 2018, 2020, 2024). A total of 1,084 radial velocity measurements were collected. Observing conditions were moderately good, but with occasional gusts resulting in the poorest seeing reaching 2.0″. To maintain the signal-to-noise ratio to reach adequate RV precision per spectra under the variable conditions, we used a mixture of 60-second and 90-second exposures, each followed by a 15-second readout, yielding cadences of 75 or 105 seconds, where the latter corresponds to a Nyquist frequency of 4800 μHz. The average time-domain scatter measured using the power density at high frequency is 0.68 m/s.

Figure 1 shows the RV time series, along with the power spectrum calculated using the Lomb-Scargle method (N. R. Lomb 1976; J. D. Scargle 1982), using the reported RV uncertainties as weights (S. Frandsen et al. 1995). We see a clear power excess around 3000 μHz. Based on a heavily smoothed power spectrum (H. Kjeldsen et al. 2008), we measured the frequency of maximum power as $\nu_{\rm max} = 3294 \pm 59$ μHz.

The oscillations observed around $\nu_{\rm max}$ are acoustic modes, and their frequencies can be well described by the asymptotic

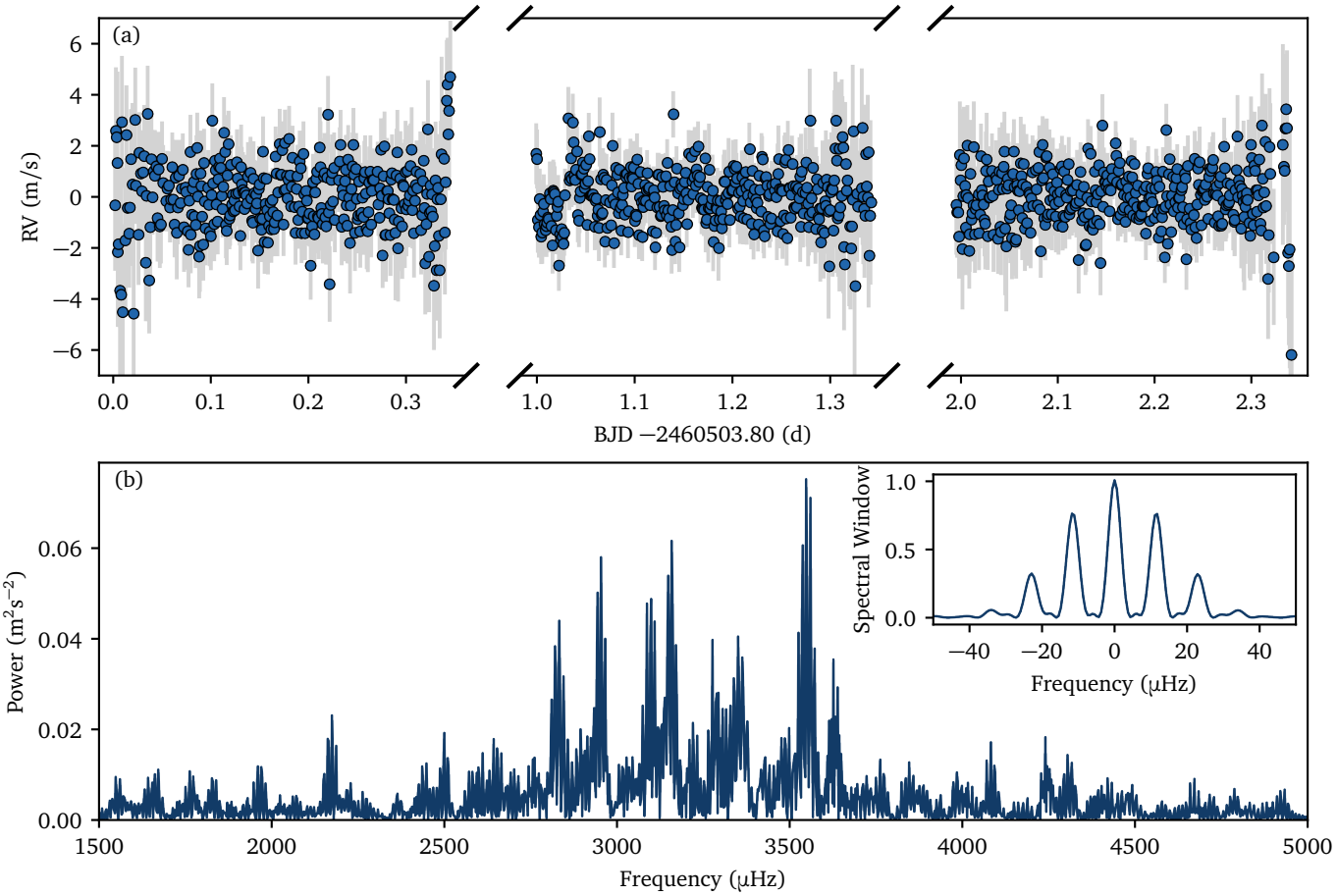

Figure 1. Radial velocity observations of HR 7672A over three consecutive nights using the Keck Planet Finder. Top: Radial-velocity time series after filtering out signals with periods longer than 1.2 hours. Bottom: Power spectrum of the RV time series, weighted by the reported RV uncertainties, displaying a clear power excess around 3000 μHz. The inset shows the spectral window.

relation involving two quantum numbers, the radial order, n, and angular degree, ℓ (M. Tassoul 1980; P. H. Scherrer et al. 1983):

$$\nu_{n,\ell} \simeq \Delta\nu\left(n + \frac{\ell}{2} + \epsilon\right) - \delta\nu_{0,\ell}. \quad (1)$$

The large frequency separation, $\Delta\nu$, depends primarily on the sound travel time across the star and, to first order, scales with the square root of the mean stellar density (R. K. Ulrich 1986). The phase offset, ϵ, generally falls between 0.8 and 1.6 in main-sequence stars (T. R. White et al. 2012), and depends on the turning points of modes (I. W. Roxburgh & S. V. Vorontsov 2003). The small separations, $\delta\nu_{0,\ell}$, quantify the frequency offsets between modes of different ℓ but with adjacent n. In main-sequence stars, $\delta\nu_{0,\ell}$ is sensitive to the chemical gradient near the core (M. Tassoul 1990; I. W. Roxburgh & S. V. Vorontsov 1994), making it a useful diagnostic for tracing hydrogen-burning processes and, therefore, for determining stellar ages on the main sequence (J. Christensen-Dalsgaard 1984; T. R. White et al. 2011; E. P. Bellinger 2019; M. Hon et al. 2024a).

To identify and measure these oscillation modes, we followed the method outlined in Y. Li et al. (2025). We applied Gold deconvolution to the power spectrum with the spectral window to reveal regular structures of mode spacings (R. Gold 1964; M. Morháč et al. 2003; Ong et al. in preparation). Figure 2(a) shows the power spectrum displayed in an échelle format, which involves folding into segments of $\Delta\nu$ and stacking them vertically (the échelle is duplicated for clarity). Figure 2(b) shows the deconvolved spectrum, revealing clear ℓ = 0–3 mode ridges, corresponding to the regular spacings dictated by Equation 1. These are more apparent in Figure 2(c), which shows the collapsed power spectrum from summing power along the vertical direction in Figure 2(b).

From Figures 2(b) and (c), we can identify the peaks along each ridge, which we preliminarily considered as candidate oscillation modes. We simultaneously fitted sine waves at these frequencies to the RV time series, obtaining the corresponding amplitudes and phases. Modes with amplitudes exceeding 3.5 times the average noise amplitude at high frequencies (0.03 m/s) were retained in the final list of modes. These are highlighted in Figure 2(d).

We also corrected the line-of-sight Doppler shifts for these frequencies following G. R. Davies et al. (2014), using a radial velocity of 5.6685 km/s based on an average value over

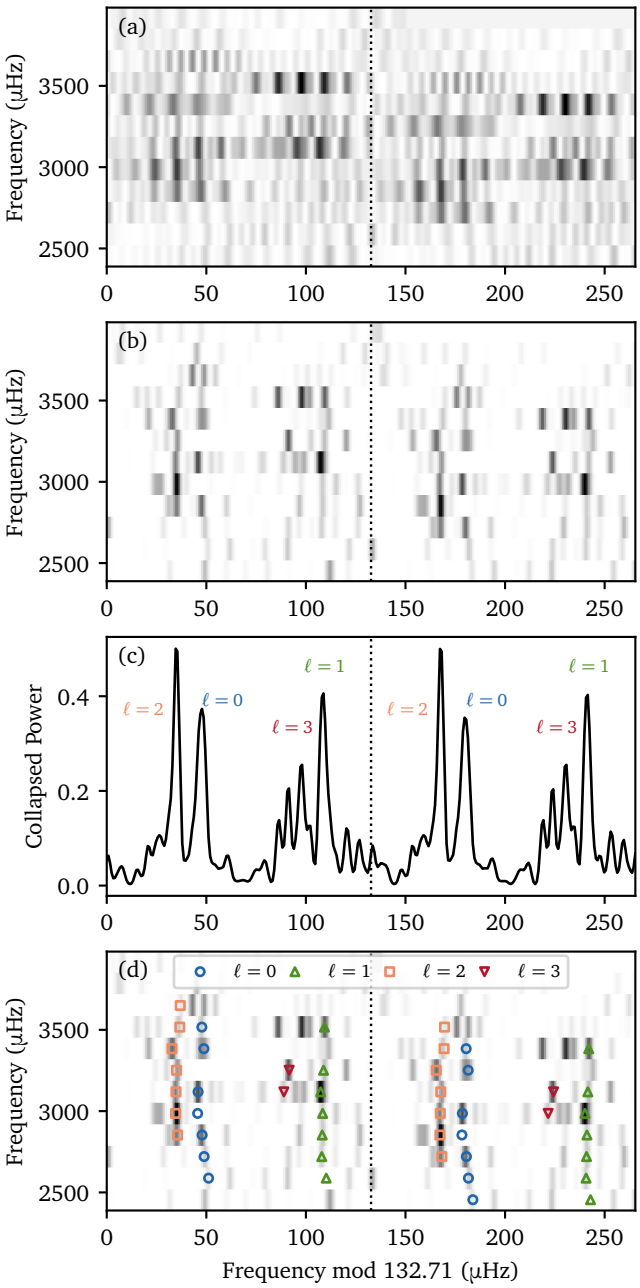

Figure 2. Replicated échelle diagrams showing structures of regular frequency spacings from KPF data. (a): échelle diagrams of the original power spectrum. (b): échelle diagram after deconvolving with the spectral window and then smoothing with a 1 μHz-width Gaussian filter. (c): collapsed échelle diagram, obtained by summing the power along the y-axis of panel b. (d): same as panel b, but highlighting the extracted oscillation modes.

three nights. The final list of frequencies are shown in Table 1. We also fitted Equation 1 to these frequencies and obtained the following asymptotic parameters: $\Delta\nu = 132.798 \pm 0.122\,\mu$Hz, $\epsilon = 1.336 \pm 0.022$, $\delta\nu_{0,1} = 5.43 \pm 0.69\,\mu$Hz, $\delta\nu_{0,2} = 12.45 \pm 0.64\,\mu$Hz, and $\delta\nu_{0,3} = 22.80 \pm 1.16\,\mu$Hz.

Table 2. Relative astrometry of HR 7672AB from direct imaging, including separations (ρ) and position angles (PA).

Date	ρ	$\sigma(\rho)$	PA	σ(PA)	Reference
	arcsec	arcsec	deg	deg	
2001.64	0.786	0.006	157.9	0.5	M. C. Liu et al. (2002)
2001.94	0.794	0.005	157.3	0.6	M. C. Liu et al. (2002)
2002.54	0.788	0.006	156.6	0.9	A. Boccaletti et al. (2003)
2006.69	0.750	0.080	155.0	5.0	E. Serabyn et al. (2009)
2007.73	0.742	0.035	151.8	2.9	J. R. Crepp et al. (2012)
2011.37	0.519	0.006	147.1	0.5	J. R. Crepp et al. (2012)
2024.78	0.852	0.007	329.5	1.1	§2.2

Table 3. Absolute astrometry of HR 7672A from Hipparcos and Gaia DR3, including proper motions in right ascension direction (μ_α) and in declination direction (μ_δ).

Date	μ_α	$\sigma(\mu_\alpha)$	μ_δ	$\sigma(\mu_\delta)$	Reference
	mas/yr	mas/yr	mas/yr	mas/yr	
1991.25	-394.07	0.63	-406.42	0.64	ESA (1997)
2016.00	-387.472	0.037	-419.497	0.030	Gaia Collaboration (2022)

2.2. *Dynamical Orbit*

HR 7672A and B form a binary system, and their mutual orbit enables a dynamical determination of the masses of both the primary star and the brown dwarf. To model the orbit and constrain the component masses, we combined astrometry with long-baseline radial velocity (RV) measurements.

Relative astrometry of the system from direct imaging has been reported in previous studies (M. C. Liu et al. 2002; A. Boccaletti et al. 2003; E. Serabyn et al. 2009; J. R. Crepp et al. 2012). We also obtained a new epoch of direct imaging with the Keck II facility imager NIRC2 on 2024 Oct 11 UT. We used its narrow camera mode (9.971 ± 0.004 mas pix^{-1}) with the standard MKO K-band filter (A. T. Tokunaga et al. 2002) for deep images and the narrow-band Brγ filter ($\lambda_{\rm cen} = 2.15762\,\mu$m) for shallow images. All images were obtained with the 256×264 subarray to achieve shorter exposure times. We performed standard bias subtraction and flat fielding corrections on all images, using 0.021-s matching subarray biases scaled to our actual exposure time of 0.05 s and K_s-band dome flats for all images.

In the deep images, the primary was saturated but the companion was well-detected, while in the shallow images, only the unsaturated primary was well-detected. We thus chose to use the shallow images, which bracketed the deep images in time, as a reference PSF image that we cross-correlated with both the primary and secondary in the deep images. Before doing so, we masked the core of the saturated primary PSF,

excluding any pixels within 3.4 pixels of the central pixel. We also attempted to remove any systematic effects of the primary's PSF wings by subtracting the median radial profile of the primary. To correct for NIRC2's geometric distortion, we placed our (x, y) coordinates of the primary (i.e., its central pixel) and companion (i.e., the primary's coordinates with the offset computed from our cross-correlation analysis) in the full 1024×1024 NIRC2 coordinate system. We used the astrometric calibration of M. Service et al. (2016) and also applied corrections from differential aberration and atmospheric refraction using the same method as described by T. J. Dupuy et al. (2016). We assumed a K-band effective wavelength of $2.18932\,\mu$m for the primary and $2.19762\,\mu$m for the secondary.

Our new measurement, along with all available measurements, are summarized in Table 2. In addition, HR 7672 A has absolute astrometry from both Hipparcos (ESA 1997) and Gaia (Gaia Collaboration 2022), allowing us to measure its proper motion acceleration over a 20-year baseline. These data are listed in Table 3.

The California Planet Search (CPS) has acquired RVs of HR 7672A from 1970 to 2024 using Lick/APF and Keck/HIRES instruments (D. A. Fischer et al. 2014; L. J. Rosenthal et al. 2021). All RVs are compiled in §A.

We modeled the dynamical orbit by jointly fitting the Hipparcos and Gaia astrometry, direct imaging measurements, and RV data. We used open source package `orvara` (T. D. Brandt et al. 2021), which performs a parallel-tempering Markov Chain Monte Carlo (MCMC) fitting. In total, our analysis used 16 free parameters. Two of them are the masses of the primary star ($M_{\rm A}$) and brown dwarf companion ($M_{\rm B}$). Six orbital parameters define the orbit of companion: semi-major axis (a_B), inclination (i_B), longitude of the ascending node (Ω_B), mean longitude at a reference epoch ($t_{\rm ref}$) of 2455197.5 JD ($\lambda_{\rm ref}$), and the eccentricity (e_B) and the argument of periastron (ω_B) in the form of $e_B \sin\omega_B$ and $e_B \cos\omega_B$. We also included four parameters to fit the zero-point for RV data from different instruments. Finally, we have four parameters for the intrinsic jitter of RV data from different instruments. Because HIRES underwent an instrument upgrade in August 2014, we adopted separate radial velocity zero points and jitters for data taken before and after the upgrade. The likelihood was computed by comparing the observed separations, position angles, absolute astrometry, and radial velocities with those predicted from a synthetic orbit, under the assumption of Gaussian measurement errors.

We used 100 walkers to sample our model and the chains converged after 2.5×10^5 steps. We discarded the first 30% as burn-in portion. The best-fitting results to the astrometric and RV data are presented in §B. In particular, we determined a primary-star mass of 1.11 ± 0.02 $M_\odot$, and a companion mass of 75.4 ± 0.7 $M_{\rm Jup}$. For comparison, J. R. Crepp et al. (2012) reported a companion mass of $68.7 \pm 2.8 M_{\rm Jup}$, T. D. Brandt et al. (2019) obtained $72.7 \pm 0.8 M_{\rm Jup}$, F. Feng et al. (2021) found $72.8 \pm 6.1 M_{\rm Jup}$, and Q. An et al. (2025) derived $71.43 \pm 1.05 M_{\rm Jup}$ (astrometry only). The difference primarily results from the inclusion of updated radial velocity and astrometric data.

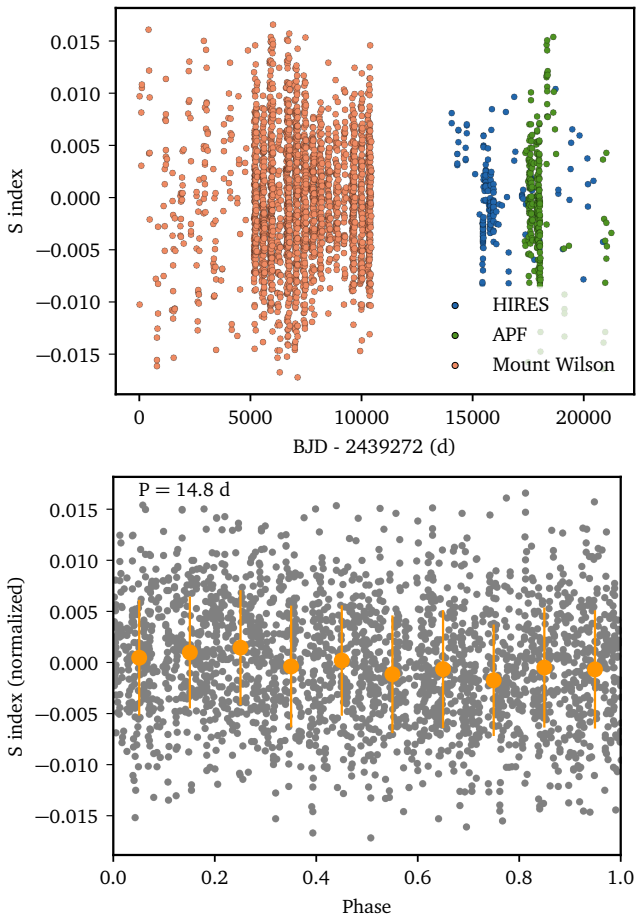

Figure 3. Top: Time series of S-index measured from Ca H & K emissions, showing a rotation period of approximately 14.2 days and a long term activity cycle. Bottom: Phase folded and normalized S-index measurements for the Mount Wilson data, showing the rotational signal. Note that the long term trend has been removed.

2.3. *Rotation and Activity*

HR 7672A has a rather long coverage of S-index over a baseline of many years, from the Mount Wilson program (R. Radick & A. Pevtsov 2018), and later coverage by Lick/APF, and Keck/HIRES. Figure 3 shows the time series of the S indices after pre-processing, which involved removal of the long term (> 1000 d) trend, subtraction of the median S index per instrument, and a 3σ clipping. The power spectra of the S index for each instrument show a clear signal at approximately 15 days for both the HIRES and Mount Wilson data. We are unable to discern a signal above the noise level in the sparsely sampled APF data and so it is not included in the following rotation analysis.

To obtain a rotation period from the S index, which is modulated by the star's rotation, we modeled the time series using a hierarchical model and Gaussian processes (D. Foreman-Mackey 2018). Each time series was assigned a single ro-

tation period, with all periods assumed to follow a normal distribution with a common mean and a standard deviation, using the rotation kernel term in CELERITE2. This rotation kernel is a sum of two simple harmonic oscillator kernels (c.f., D. Foreman-Mackey 2018). A hierarchical model is well suited in this situation because of varying systematics, noise levels, and signal amplitudes across instruments. Using this model, we determined a rotation period of $P_{\rm rot}$ = 14.8 ± 1.3 d. This value agrees well with the rotation periods derived in previous work such as 13.94 d from R. A. Donahue et al. (1996) from Mount Wilson data alone, and 13.95 d from S. Messina et al. (2001) from V-band photometry, and 14.54 d from Keck/HIRES.

We also checked if there is any signature of rotation in TESS photometry, which has observed this star in Sector 58 and 81. We found a cyclic modulation on the order of 6.27 d, which is about half of what S-indices suggests. This is expected in short photometric time series, where harmonics of the true rotation period are often seen as a signature of active regions emerging in different longitude.

The average S-index of 0.19 corresponds to a $\log R'_{\rm HK}$ value of -4.74 (S. Boro Saikia et al. 2018), placing the star firmly within an active regime where standard magnetic spin-down remains applicable. Weakened magnetic braking is only expected to commence when $\log R'_{\rm HK}$ reaches -5.0, or equivalently, at a Rossby number of 0.9Ro$_\odot$ (J. L. van Saders et al. 2016; N. Saunders et al. 2024).

Given the measured rotation period, the expected rotational splittings between $-\ell \le m \le \ell$ are 1.64, 3.28, and 4.92 μHz for $\ell = 1, 2, 3$ modes, respectively. Indeed, some broadening is observed in the ridges formed by non-radial modes in Figure 2(b), which could plausibly be attributed to this rotational splitting.

2.4. *Effective Temperature and Metallicity*

To determine the spectroscopic parameters, including effective temperature $T_{\rm eff}$ and metallicity [M/H], we adopted the values from L. J. Rosenthal et al. (2021), derived from Keck/HIRES spectra. They are 5932 K and 0.051 dex, respectively. We also compiled $T_{\rm eff}$ and [M/H] values in literature using the SIMBAD astronomical database. These values exhibit a spread of around 100 K in $T_{\rm eff}$ and 0.1 dex in [M/H], which we adopt as the representative uncertainties. These are consistent with typical spectroscopic uncertainties for solar-type stars (A. Serenelli et al. 2017; J. Tayar et al. 2022).

2.5. *Luminosity*

We used `isoclassify` (D. Huber et al. 2017; T. A. Berger et al. 2020) to calculate the bolometric flux based on apparent magnitudes from the Tycho-2, Gaia, and 2MASS photometric systems. Combined with the Gaia DR3 distance (C. A. L. Bailer-Jones et al. 2021), this yields an estimate of the stellar luminosity. Depending on the band used, the derived luminosity ranges from 1.0 to 1.75 L$_\odot$, with typical formal uncertainties of approximately 0.04 L$_\odot$. The large spread reflects systematic issues such as saturation in bright-star photometry, uncertainties in bolometric corrections, and photometric zero points (M. Riello et al. 2021). The Gaia BP and RP bands are the most discrepant. Among the available bands, the luminosity value based on the 2MASS K_s band appears most consistent with that derived from asteroseismic modeling in §3.1. However, we did not use it as a modeling constraint due to the inconsistency across photometric bands. All stellar parameters are summarized in Table 5.

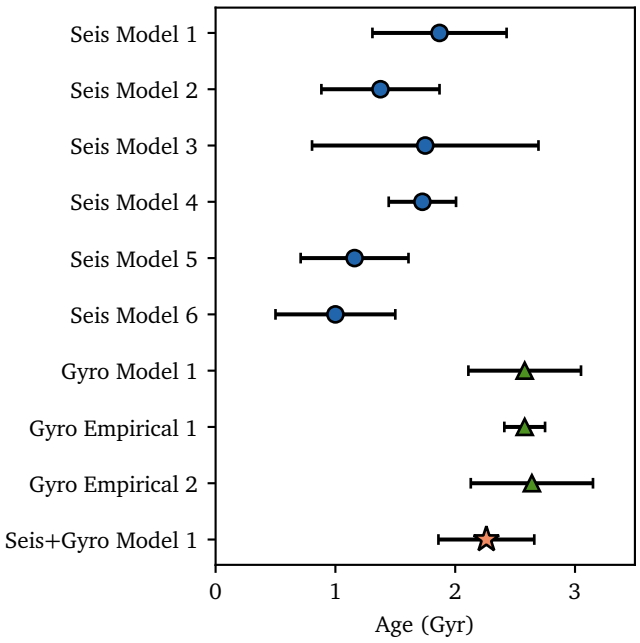

Figure 4. Estimates of stellar ages derived from various methods, including six asteroseismic modeling ages, one rotational modeling age, two rotational empirical ages, and one asteroseismic and rotational joint modeling age.

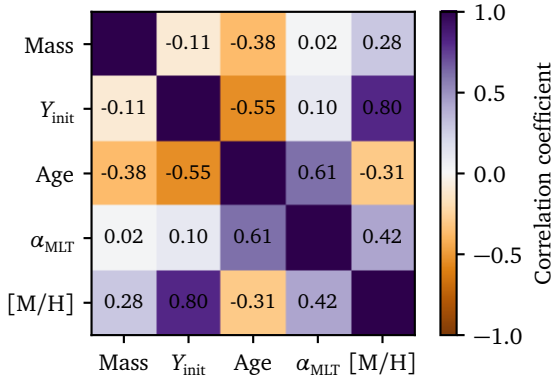

Figure 5. Correlation coefficients of stellar model input parameters $\mathbf{x} = (M, Y_{\rm init}, {\rm Age}, \alpha_{\rm MLT}, [{\rm M/H}])$ constrained using asteroseismology, estimated from models implemented by Team 1.

Table 4. Summary of the frequency modeling.

	Team 1	Team 2	Team 3	Team 4	Team 5	Team 6
Model Configuration						
Stellar evolution code	MESA r240301	MESA r12778	GARSTEC v2015	YREC	GARSTEC v2020	ASTEC
Pulsation code	GYRE v7.1	GYRE v5	ADIPLS v0.4	H. M. Antia & S. Basu (1994)	GYRE v7.2	ADIPLS
Opacities & EOS	OPAL	OPAL	OPAL	OPAL	OPAL	OPAL
Atmospheric boundary condition	P. H. Hauschildt et al. (1999a,b) F. Castelli & R. L. Kurucz (2003)	K. S. Krishna Swamy (1966)	A. S. Eddington (1926)	A. S. Eddington (1926)	R. Trampedach et al. (2014)	A. S. Eddington (1926)
Metal mixture	M. Asplund et al. (2009)	M. Asplund et al. (2009)	M. Asplund et al. (2009)	N. Grevesse & A. J. Sauval (1998)	N. Grevesse & A. J. Sauval (1998)	N. Grevesse & A. J. Sauval (1998)
Nuclear reaction rate	R. H. Cyburt et al. (2010) C. Angulo et al. (1999)	R. H. Cyburt et al. (2010) C. Angulo et al. (1999)	C. Angulo et al. (1999) A. Formicola et al. (2004) J. W. Hammer et al. (2005)	E. G. Adelberger et al. (1998) A. Formicola et al. (2004)	C. Angulo et al. (1999) A. Formicola et al. (2004) J. W. Hammer et al. (2005)	C. Angulo et al. (1999)
Mixing length formulation	L. Henyey et al. (1965)	J. P. Cox & R. T. Giuli (1968)	E. Böhm-Vitense (1958)	E. Böhm-Vitense (1958)	J. P. Cox & R. T. Giuli (1968)	E. Böhm-Vitense (1958)
Mixing length parameter $\alpha_{\rm MLT}$	Free	Solar-calibrated	Free	Free	Varying vs. solar-calibrated	Free
$\alpha_{\rm MLT,\odot}$	1.96	1.71	1.79	1.84	1.83	2.12
Convective overshoot	F. Herwig (2000) $f_{\rm ov,shell} = 0.0174$	None	None	None	None	None
Extra-mixing	None	Gravitational settling Turbulent mixing	A. A. Thoul et al. (1994)	A. A. Thoul et al. (1994)	A. A. Thoul et al. (1994) Diffusive mixing	G. Michaud & C. R. Proffitt (1993)
Surface correction	W. H. Ball & L. Gizon (2014) two-term +Y. Li et al. (2023) ensemble correction	T. Sonoi et al. (2015)	W. H. Ball & L. Gizon (2014) cubic-term	W. H. Ball & L. Gizon (2014) two-term	W. H. Ball & L. Gizon (2014) two-term + I. W. Roxburgh (2016) ϵ-matching	H. Kjeldsen et al. (2008)
Grid free parameters	M, [M/H], $\alpha_{\rm MLT}$, $Y_{\rm init}$	M, [M/H], $Y_{\rm init}$	M, [M/H], $\alpha_{\rm MLT}$, $Y_{\rm init}$	M, [M/H], $\alpha_{\rm MLT}$, $Y_{\rm init}$	M, [M/H], $Y_{\rm init}$	M, [M/H], $\alpha_{\rm MLT}$, $Y_{\rm init}$
Derived Stellar Parameters						
Mass $M_\star$ ($M_\odot$)	1.114 ± 0.013	1.111 ± 0.017	1.110 ± 0.015	1.106 ± 0.016	1.110 ± 0.016	1.110 ± 0.030
Radius $R_\star$ ($R_\odot$)	1.051 ± 0.004	1.047 ± 0.006	1.049 ± 0.006	1.076 ± 0.007	1.050 ± 0.007	1.048 ± 0.009
Age $t_\star$ (Gyr)	1.869 ± 0.560	1.376 ± 0.493	1.750 ± 0.945	1.726 ± 0.281	1.160 ± 0.450	1.000 ± 0.500
Density $\rho_\star$ ($\rho_\odot$)	0.960 ± 0.002	0.966 ± 0.006	0.962 ± 0.006	0.892 ± 0.021	0.957 ± 0.013	0.964 ± 0.004
Surface gravity $\log g_\star$ (dex)	4.442 ± 0.002	4.443 ± 0.003	4.442 ± 0.002	4.416 ± 0.004	4.440 ± 0.004	4.443 ± 0.003
$Y_{\rm init}$	0.246 ± 0.017	0.276 ± 0.016	0.258 ± 0.016	0.274 ± 0.009	0.267 ± 0.011	0.269 ± 0.016
$\alpha_{\rm MLT}/\alpha_{\rm MLT,\odot}$	1.046 ± 0.053	—	1.004 ± 0.072	0.903 ± 0.047	—	0.953 ± 0.066

Table 5. Stellar properties of HR 7672A (15 Sge; HD 190406; HIP 98819).

Property	Value	Reference
Photometry		
K_s-band magnitude	4.388 ± 0.027	R. M. Cutri et al. (2003)
Dynamical Orbit		
Mass ($M_\odot$)	1.111 ± 0.017 [1,2]	§2.2
Mass (M_{Jup}; HR 7672 B)	75.39 ± 0.67	§2.2
Astrometry		
Distance (pc)	11.758 ± 0.014	C. A. L. Bailer-Jones et al. (2021)
Luminosity $L_\star$ ($L_\odot$)	1.224 ± 0.043	§2.5
Spectroscopy		
Effective temperature $T_{\rm eff}$ (K)	5932 ± 81 [1,2]	L. J. Rosenthal et al. (2021)
Metallicity [Fe/H] (dex)	0.051 ± 0.057 [1,2]	L. J. Rosenthal et al. (2021)
Asteroseismology		
$\nu_{n,\ell}$ (μHz)	Table 1 [1]	§2.1
ϵ	1.335 ± 0.023	§2.1
$\Delta\nu$ (μHz)	132.806 ± 0.126	§2.1
$\delta\nu_{0,1}$ (μHz)	5.47 ± 0.69	§2.1
$\delta\nu_{0,2}$ (μHz)	12.53 ± 0.67	§2.1
$\delta\nu_{0,3}$ (μHz)	22.87 ± 1.17	§2.1
$\nu_{\rm max}$ (μHz)	3294 ± 59	§2.1
$A_{\rm osc}$ (cm s^{-1})	17.34 ± 1.59	§2.1
Mass ($M_\odot$)	1.114 ± 0.013 (stat) ± 0.002 (sys)	§3.1
Radius ($R_\odot$)	1.051 ± 0.004 (stat) ± 0.010 (sys)	§3.1
Luminosity ($L_\odot$)	1.25 ± 0.05 (stat) ± 0.01 (sys)	§3.1
Asteroseismic age (Gyr)	1.87 ± 0.56 (stat) ± 0.32 (sys)	§3.1
Density ($\rho_\odot$)	0.960 ± 0.002 (stat) ± 0.026 (sys)	§3.1
$\log g$ (cgs; dex)	4.442 ± 0.002 (stat) ± 0.010 (sys)	§3.1
Rotation		
Rotation period $P_{\rm rot}$ (d)	14.8 ± 1.3 [2]	§2.3
Rotational age (Gyr)	2.58 ± 0.47	§3.2
Asteroseismology + Rotation		
Asteroseismic + rotational joint age (Gyr)	2.26 ± 0.40	§3.3

Note—1. Used for asteroseismic modeling. 2. Used for rotational modeling.

3. STELLAR AGES

3.1. *Asteroseismic Modeling*

To estimate the stellar age from oscillation frequencies, we used six independent modeling pipelines. This approach allows us to assess systematic uncertainties associated with differences in input physics and modeling codes.

Stellar evolution codes used by the six teams included MESA (B. Paxton et al. 2011, 2013, 2015, 2018, 2019; A. S. Jermyn et al. 2023; N. Moedas et al. 2024), GARSTEC (A. Weiss & H. Schlattl 2008), YREC (P. Demarque et al. 2008), and ASTEC (J. Christensen-Dalsgaard 2008a). Pulsation codes used for calculating oscillation frequencies included GYRE (R. H. D. Townsend & S. A. Teitler 2013), ADIPLS (J. Christensen-Dalsgaard 2008b), and H. M. Antia & S. Basu (1994).

The input physics used by the six teams also differed. Treatments of atmospheric boundary conditions included the Eddington (A. S. Eddington 1926) and Krishna-Swamy (K. S. Krishna Swamy 1966) T-τ relations, and precomputed photosphere tables (P. H. Hauschildt et al. 1999a,b; F. Castelli & R. L. Kurucz 2003; R. Trampedach et al. 2014). Choices of nuclear reaction rates varied from R. H. Cyburt et al. (2010), C. Angulo et al. (1999), A. Formicola et al. (2004), J. W. Hammer et al. (2005), and E. G. Adelberger et al. (1998). The mixing length formulations included L. Henyey et al. (1965), J. P. Cox & R. T. Giuli (1968) and E. Böhm-Vitense (1958), with some teams using solar-calibrated mixing length parameters, others treating it as a free variable, and still others using calibrated prescriptions for varying it. Two main metal mixtures were used: those of M. Asplund et al. (2009) and of N. Grevesse & A. J. Sauval (1998). Mass, metallicity, and initial helium abundance were all treated as free parameters by all teams.

Different teams employed different correction procedures for near-surface modeling errors. Several of the teams used empirical correction formulae (H. Kjeldsen et al. 2008; W. H. Ball & L. Gizon 2014), where an offset is applied to the mode frequencies to account for the effects of the surface term, before the corrected mode frequencies are used to construct a conventional likelihood function. These empirical formulae admit additional free parameters, which may either be fitted against the data, or potentially be externally calibrated against 3D models (T. Sonoi et al. 2015) or from an empirical ensemble (Y. Li et al. 2023). Other teams employed the nonparametric ϵ-matching technique (I. W. Roxburgh 2016), where combinations of mode frequencies are computed from both the model and observed set, chosen so that the likelihood function evaluated from these combinations is insensitive to the near-surface structure of the star (J. M. J. Ong et al. 2021). Table 4 lists the detailed configurations as well as the derived stellar parameters by each team.

Overall, the derived stellar properties for HR 7672A show consistency across modeling teams, despite intentional variations in input physics. The standard deviation of median values from each team is comparable to or smaller than the average uncertainties reported by each team, indicating that model uncertainties arising from differences in input physics and stellar evolution codes are generally smaller than the formal uncertainties reported.

We report our stellar properties of HR 7672A as follows: we adopted the median values and the statistical uncertainties from Team 1's median and formal uncertainty, and adopted the standard deviation of the median values reported by the different teams as an estimate of the systematic uncertainties. The results are reported in Table 5. We find a radius of $R_\star$ = 1.051 ± 0.004 (stat) ± 0.010 (sys) $R_\odot$, a luminosity of $L_\star$ = 1.25 ± 0.05 (stat) ± 0.01 (sys) $L_\odot$, and an age of $t_\star$ = 1.87 ± 0.56 (stat) ± 0.32 (sys) Gyr, based on asteroseismology.

3.2. *Rotational Modeling*

To model the star based on its rotation period using gyrochronology, we require rotation period predictions from stellar models. For this purpose, we used Team 1's stellar models in combination with the `rotevol` code (J. L. van Saders & M. H. Pinsonneault 2013; G. Somers et al. 2017). Angular momentum loss was modeled using a calibrated prescription, based on open cluster data and asteroseismic field stars, following the configuration described in Y. Li et al. (2025).

We briefly summarize the calibration procedure used in the angular momentum loss modeling. Stellar models were initialized with a rotation period of $P_{\rm disk}$ = 4 days and a disk-locking timescale of $\tau_{\rm disk}$ = 10 Myr, following the setup of F. Chiti et al. (2024). Angular momentum loss was modeled using the prescription from J. L. van Saders et al. (2016), which relates the loss rate to the stellar rotation rate and convective overturn timescale, scaled by a braking efficiency parameter f_K. When the Rossby number exceeds a critical threshold $\mathrm{Ro}_{\rm crit}$, the star enters a weakened magnetic braking regime, and angular momentum loss is no longer applied. This is less relevant in our case because the star has not entered into that phase. Stellar rotation was modeled using a two-zone framework in which the radiative core and convective envelope rotate as solid bodies but exchange angular momentum over a coupling timescale $\tau_{\rm ce}$. This timescale is assumed to scale with stellar mass as $\tau_{\rm ce}/\tau_{\rm ce,\odot} = (M/M_\odot)^{-\alpha_{\rm ce}}$, where $\tau_{\rm ce,\odot} \approx 22$ Myr (F. Spada & A. C. Lanzafame 2020). The free parameters in the model — f_K, $\mathrm{Ro}_{\rm crit}$, and $\alpha_{\rm ce}$ — were calibrated to reproduce the rotation periods of stars in a set of well-characterized open clusters (L. M. Rebull et al. 2016; S. T. Douglas et al. 2017, 2019; J. L. Curtis et al. 2019; S. Meibom et al. 2015; J. L. Curtis et al. 2020; S. A. Barnes et al. 2016; R. Dungee et al. 2022; L. Long et al. 2023), asteroseismic field stars (O. J. Hall et al. 2021; V. Silva Aguirre et al. 2015, 2017), and the Sun (J. N. Bahcall et al. 1995) at their respective ages.

The models calculated by Team 1 are described by the input parameters $\mathbf{x} = (M, Y_{\rm init}, \mathrm{Age}, \alpha_{\rm MLT}, [\mathrm{M/H}])$. Following calibration, each model can be assigned with a rotation period. Then we fitted these models with observational constraints $\mathbf{D}$. We constructed a χ^2 statistic using stellar mass, rotation period, effective temperature, and metallicity, lead-

ing to a posterior probability of the form:

$$\begin{aligned}\ln p(\mathbf{x} \mid \mathbf{D}) \propto -\frac{1}{2}\Big[&(M_{\rm mod} - M_{\rm obs})^2 / \sigma_M^2 \\ &+ \left(T_{\rm eff,mod} - T_{\rm eff,obs}\right)^2 / \sigma_{T_{\rm eff}}^2 \\ &+ ([{\rm M/H}]_{\rm mod} - [{\rm M/H}]_{\rm obs})^2 / \sigma_{[{\rm M/H}]}^2 \\ &+ \left(P_{\rm rot,mod} - P_{\rm rot,obs}\right)^2 / \sigma_{P_{\rm rot}}^2 \Big].\end{aligned} \tag{2}$$

Any other model parameter θ to be estimated can be obtained by marginalization:

$$p(\theta \mid \mathbf{D}) = \int \delta(\theta - \theta(\mathbf{x}))\; p(\mathbf{x} \mid \mathbf{D})\; {\rm d}\mathbf{x}, \tag{3}$$

where δ is the Kronecker delta function. We report the result using the median and the 16th and 84th percentile credible intervals. From this, we determined a rotation-based age of $\tau_\star = 2.58 \pm 0.47$ Gyr.

In addition to this physics-based approach, which models stellar rotation using an angular momentum loss prescription, we also consider empirical rotation-age-temperature relations, which are more data-driven. We adopted two empirical models. The `gpgyro` model (Y. Lu et al. 2024) calibrates the spin-down relation using stellar clusters and kinematic ages. For this star, it predicts an age of 2.58 ± 0.17 Gyr, using $P_{\rm rot}$, $T_{\rm eff}$, and the absolute Gaia G-band magnitude as inputs. The `gyrointerp` model (L. G. Bouma et al. 2024) is calibrated on stellar clusters and predicts an age of 2.64 ± 0.51 Gyr, based on $P_{\rm rot}$ and $T_{\rm eff}$. The larger uncertainty in the latter estimate likely reflects a more realistic treatment of the intrinsic spread in gyrochrones, with considerations for the empirical limits of gyrochronology.

These rotation-based age estimates are listed in Table 5. A comparison of all estimates is shown in Figure 4, where we find that the results are broadly consistent across methods. However, the rotation-based ages tend to be systematically higher than those derived from asteroseismology, although the difference is not statistically significant. This offset could arise from systematic effects in either method. For example, latitudinal differential rotation can limit the accuracy of rotation-based estimates (C. R. Epstein & M. H. Pinsonneault 2014), while uncertainties in the initial helium abundance can affect the seismic diagnostics of the sound-speed profile. To mitigate such systematics, a more robust approach is to perform a joint modeling of both methods, which we explore next.

3.3. *Asteroseismic and Rotational Joint Modeling*

Since Team 1's models include both oscillation frequencies and rotation periods as outputs, we use this opportunity to jointly model the star using both asteroseismic and rotational constraints. We also aim to account for systematic uncertainties of ages arising from uncertainties in the underlying stellar physics adopted by a single modeling pipeline.

For this purpose, we introduce a workflow that incorporates systematic uncertainties in age estimation during the modeling process, while still combining both asteroseismic and rotational constraints. In the asteroseismic analysis, under constraints on $T_{\rm eff}$, [M/H], mass, and oscillation frequencies, we can approximate the posterior distributions of the model input parameters $\mathbf{x}$ using a multivariate Gaussian distribution with a mean of μ and covariance Σ, such that $p(\mathbf{x}) \sim \mathcal{N}(\mu, \Sigma)$. In Figure 5, we show the standardized correlation coefficient matrix, which reveals strong correlations among several model parameters. The diagonal elements of the covariance matrix, in particular, quantify the uncertainties in each parameter within the context of Team 1's model grid. To incorporate systematic uncertainty in age, we computed the spread in seismic ages across all modeling teams and inflate the variance of stellar age (i.e., the diagonal element corresponding to age) by adding this systematic component in quadrature.

To perform the joint fit using both asteroseismic and rotational constraints, we treated the multivariate Gaussian distribution of the model input parameters $\mathbf{x}$ from the asteroseismic analysis, $\mathcal{N}(\mu, \Sigma)$, as a prior, and adopted the observed rotation period as an observational constraint to include in the likelihood function. The resulting posterior probability for the model parameter is:

$$\begin{aligned}\ln p(\mathbf{x} \mid \mathbf{D}) &\propto \ln p(\mathbf{x}) + \ln p(\mathbf{D} \mid \mathbf{x}) \\ &= -\frac{1}{2}(\mathbf{x} - \mu)^T \mathbf{\Sigma}^{-1} (\mathbf{x} - \mu) \\ &= -\frac{1}{2}\left(P_{\rm rot,mod} - P_{\rm rot,obs}\right)^2 / \sigma_{P_{\rm rot}}^2.\end{aligned} \tag{4}$$

We obtained a final age estimate of $t_\star = 2.26 \pm 0.40$ Gyr. The joint estimate falls between the asteroseismic and rotational ages, with an uncertainty of 18%. These results are summarized in Table 5 and shown in Figure 4. For comparison, J. R. Crepp et al. (2012) estimated the system age to be 2.5 ± 1.8 Gyr from isochrone fitting and 2.5 ± 0.7 Gyr from gyrochronology relations using E. E. Mamajek & L. A. Hillenbrand (2008). The combination of asteroseismology and gyrochronology employed in this work relies on independent diagnostics, making the resulting age scale more accurate and less affected by method-specific systematics. We also find an improvement in precision compared to previous estimates.

4. TESTING BROWN DWARF COOLING MODELS

Our new high-precision measurements of the HR 7672B dynamical mass and the age of the HR 7627AB system, combined with the existing HR 7672B luminosity measurement, enable this benchmark system to test substellar evolutionary models with a degree of rigor previously not possible. We consider six widely-used model grids: A. Burrows et al. (1997, Burrows1997), D. Saumon & M. S. Marley (2008, SM2008), I. Baraffe et al. (2015, BHAC2015), M. W. Phillips et al. (2020b, ATMO2020), G. Chabrier et al. (2023, CBPD2023), and C. V. Morley et al. (2024, Diamond-

back). The different models employ different interior physics (e.g., equations of state) and boundary conditions (e.g., atmosphere models). Brown-dwarf evolution grids have progressed from early non-gray, baseline cooling tracks to modern models that fold in updated H/He equations of state (EOS), opacities, cloud physics, chemistry, and vertical mixing. Burrows1997 (A. Burrows et al. 1997) sets the foundation with non-gray atmospheres and coupled spectra/cooling. SM2008 (D. Saumon & M. S. Marley 2008) introduced a hybrid cloudy/clear prescription to capture the L/T transition. BHAC2015 (I. Baraffe et al. 2015) refreshed pre-main-sequence/young-BD tracks with boundary conditions based on BT-Settl model atmospheres. ATMO2020 (M. W. Phillips et al. 2020b) added a new H-He EOS and expanded opacities and chemistry. CBPD2023 (G. Chabrier et al. 2023) then isolated interior updates with a newer EOS, shifting hydrogen-burning limits and late-time cooling. Diamondback delivered a modern cloudy grid for warm L/T objects that systematically varies metallicity and cloud sedimentation. We use the solar-metallicity versions of all these models, in accord with the metallicity of HR 7672A.

Along our new dynamical mass ($M = 75.39 \pm 0.67$ M_{Jup}) and host star age ($t = 2.26 \pm 0.40$ Gyr), the third observation of HR 7672B needed to test models is the bolometric luminosity. We adopt $\log(L/L_\odot) = -4.19 \pm 0.04$ dex from T. D. Brandt et al. (2019), which represents the weighted average of values derived from the H-band (-4.23 ± 0.05 dex) and K_S-band (-4.14 ± 0.06 dex) photometry measured by A. Boccaletti et al. (2003) combined with a bolometric correction from T. J. Dupuy & M. C. Liu (2017). We note that the A. Boccaletti et al. (2003) photometry leads to a color of $(H - K_S) = 1.00 \pm 0.17$ mag, which is somewhat redder compare to colors for mid-L dwarfs, e.g., $(H - K_S) = 0.64^{+0.11}_{-0.20}$ mag from the L4–L4.9 template of W. M. J. Best et al. (2018).

Figure 6 summarizes the properties of all known substellar benchmarks with both substellar mass and system age determinations, showing how HR 7672 is distinguished by its combination of high precision in both parameters. Figure 7 provides an illustration of the evolutionary models that we consider here, constructed using the measured dynamical mass of HR 7672B — as is apparent, our new measurements are in tension with a number of the models, which we examine quantitatively below.

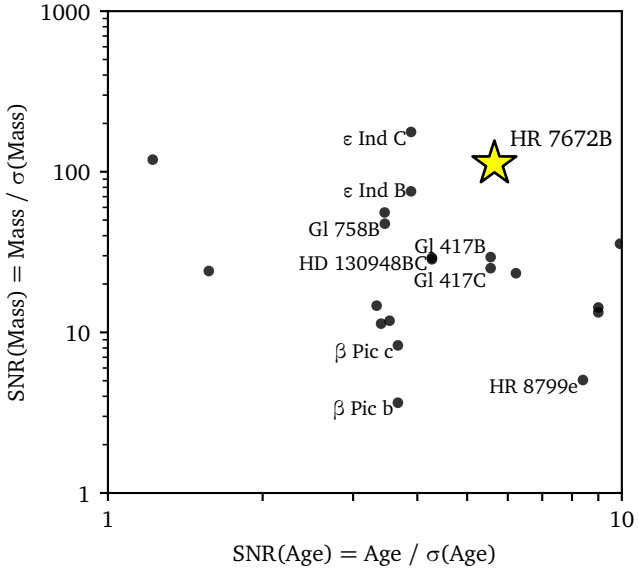

Figure 6. The signal-to-noise ratios of dynamical mass and host star age for all known substellar benchmarks. HR 7672B's high precision in both quantities (0.9% in mass and 18% in age) makes it the best known system to test brown dwarf evolutionary models.

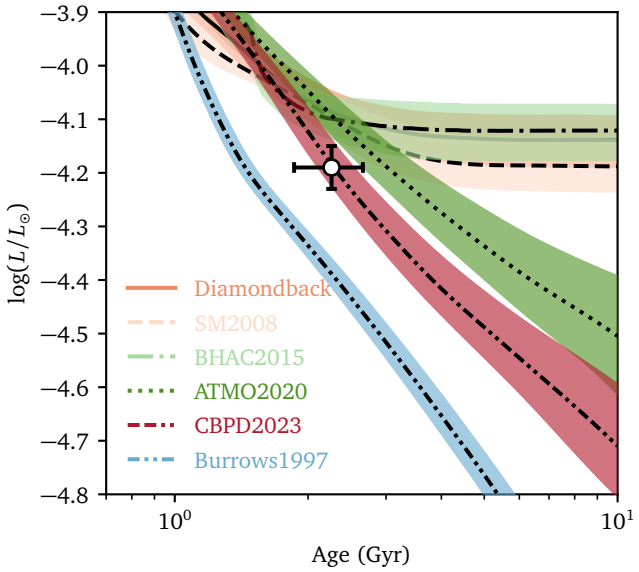

Figure 7. Brown dwarf cooling tracks from 6 evolutionary model grids for HR 7672B given its measured dynamical mass and 1-σ uncertainty. The circle indicates the observed values.

4.1. *Consistency tests among mass, age, and luminosity*

Independent measurements of mass, age, and luminosity allow any two quantities to predict the third using an evolutionary model, enabling a direct comparison between the model-predicted and observed values for the third quantity. We performed this test using the rejection-sampling procedure described in T. J. Dupuy & M. C. Liu (2017) and T. J. Dupuy et al. (2023). To obtain the model-predicted distribution of $\log L$ based on mass and age, we drew normally distributed random values for mass and age according to their observational uncertainties and calculated the corresponding luminosity for each mass-age pair through bicubic interpolation on the model grids.

Conversely, to derive the model-predicted distributions of age (or mass) given the observed distributions of $\log L$ and mass (or age), we applied a rejection-sampling method. We drew normally distributed random values for mass (or age) based on their measured uncertainties and uniformly sampled age (or mass). For each mass–age pair, we com-

puted $\log L$ using the evolutionary model. A random number u, uniformly distributed between 0 and 1, was then generated, and the rejection probability was defined as $p \propto \exp\left[-(X_{\rm obs} - X_{\rm mod})^2/\sigma_X^2\right]$, where $X = \log L$. Samples with $p < u$ were rejected, and the accepted samples were used to construct the final age (or mass) distributions.

When using $\log L$ and M to derive the model age distribution, we encountered a limitation: some models do not reach luminosities as low as the observations. As shown in Figure 7, for Diamondback, SM2008, and BHAC2015, the minimum luminosity remains higher than the observed value, though still somewhat/marginally consistent when considering the errors in the observed L and the mass. Consequently, many samples cannot find valid solutions during rejection sampling due to the restricted model space. Figure 8 illustrates this effect by showing the minimum luminosity reached by each evolutionary model as a function of mass. Each model's tracks occupy the parameter space above these lines. For Diamondback, SM2008, and BHAC2015, these boundaries lie above the observed luminosity, implying that many randomly drawn samples cannot find acceptable model counterparts. To quantify the impact, we computed a "model-coverage fraction," defined as the proportion of sampled points that fall within the bounds of physical models at 10 Gyr, based on normally sampled luminosity and mass values.

Figure 9 presents the resulting model-predicted probability distributions compared to the observed distributions for $\log L$, mass, and age. Table 6 lists the significance levels of the discrepancies between the observed and modeled values as well as the model-coverage fractions. The significance levels were derived using a nonparametric sign test. We first computed the residuals between the observational and modeled samples, then determined the fractions of positive and negative residuals. The smaller of the two fractions represents the tail probability from the side with fewer samples, which was multiplied by two to obtain the two-sided tail probability p. This probability p was then converted into an equivalent σ value using the inverse survival function of a normal distribution. For the age test, to handle models that only partly overlap the observations, we scaled the generate posterior using the model-coverage fraction, by adding a corresponding set of samples with infinite ages to produce the final posterior.

From these comparisons, we found that the Burrows1997 models predict the lowest luminosities and a clearly substellar nature for HR 7672B. The ATMO2020 model lies near the transition between the bottom of the main sequence and the brown dwarf regime, while its successor CBPD2023 shows the best agreement with our measurements and remains below the threshold for sustained hydrogen fusion. The three models that include cloud treatment through the L/T transition (BHAC2015, SM2008, and Diamondback) predict slightly higher luminosities than observed, indicating a stellar outcome for HR 7672B at the low-mass end of the main sequence given its measured dynamical mass. These

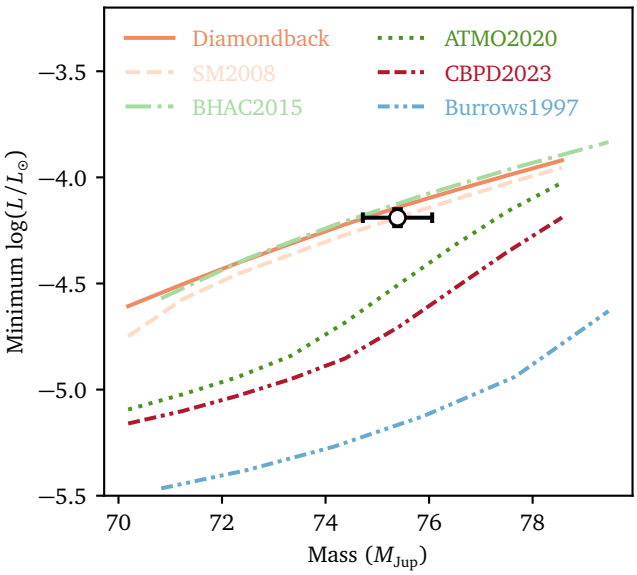

Figure 8. The minimum luminosity reached along the brown dwarf cooling tracks is shown as a function of mass. This minimum luminosity corresponds to the luminosity at the 10 Gyr age in the cooling tracks. Diamondback and SM2008 go beyond 10 Gyr, but we truncate at 10 Gyr for our tests. The evolutionary models populate only the region above the plotted lines, and the circle indicates the observed values for HR 7672B. The minimum luminosities of the Diamondback and BHAC2015 models are only marginally consistent with the observations (model-coverage fractions of 16% and 24%, respectively) and the SM2008 models also may be in tension (50% model-coverage fraction), suggesting that the stellar/substellar boundary in these models is too low in mass.

models suggest that the object would reach the zero-age main sequence in approximately 1–2 Gyr, producing the long tail in the age distribution in Figure 9 and the flattening in the cooling tracks in Figure 7. The implication for these three models is that their predicted stellar/substellar boundary is too low in mass.

Despite the differing evolutionary pathways predicted by the models for HR 7672B's mass, these predictions have not yet diverged significantly at the age of the object. As summarized in Table 6, all models remain consistent with the measurements within $\approx 2.7\sigma$.

Finally, we consider which observed quantities could most improve model discrimination (Figure 9). The age uncertainty (18%) is relatively large, and further improvements in the host star age will be challenging, given the substantial observing time needed to measured the current asteroseismic age. Moreover, an improved age is unlikely to enhance model separation, as the system lies in a region where models predict similar luminosities. The narrow substellar mass range already provides some discriminatory power, and upcoming data from Gaia DR4 can further refine the mass and improve model differentiation. A reduced luminosity uncertainty (currently 10%) would likely provide the strongest im-

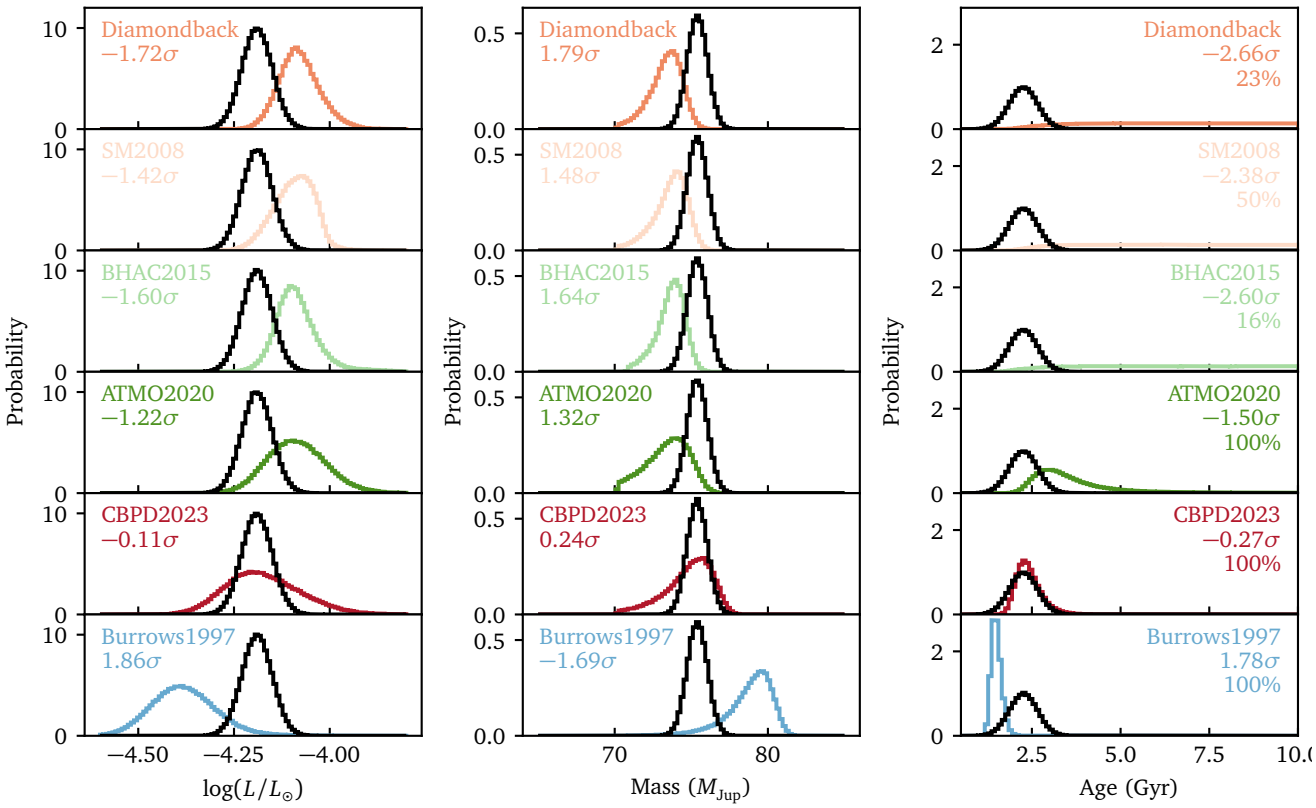

Figure 9. Comparisons between the observed and model-predicted properties of HR 7672B, where the predicted value of each property is calculated based on the other two. The black lines represent the observed distributions, and the colored lines show the model predictions. The numbers in each panel indicate the significance level of the discrepancy between the two distributions. In the rightmost column (age), the model-coverage fraction (the proportion of sampled points that lie within the bounds of physical models at 10 Gyr), is also shown.

Table 6. Significance levels of the discrepancies between the model-predicted and measured properties of HR 7672B. The signs in the first three columns indicate the direction of the discrepancy, expressed as O−C (observed−modeled).

Model	L_{obs} vs. $L_{mod}(M_{obs},t_{obs})$	M_{obs} vs. $M_{mod}(L_{obs},t_{obs})$	t_{obs} vs. $t_{mod}(M_{obs},L_{obs})$ (model-coverage fraction)	D^2
Diamondback	-1.71σ	1.78σ	-2.66σ (0.226)	1.63σ
SM2008	-1.42σ	1.48σ	-2.38σ (0.509)	1.31σ
BHAC2015	-1.61σ	1.62σ	-2.58σ (0.170)	1.54σ
ATMO2020	-1.22σ	1.32σ	-1.51σ (0.998)	1.15σ
CBPD2023	-0.11σ	0.25σ	-0.27σ (1.000)	0.06σ
Burrows1997	1.86σ	-1.68σ	1.78σ (1.000)	1.92σ

provement, as it could distinguish between the higher-mass substellar boundary predicted by ATMO2020 and the lower-mass boundary suggested by models such as SM2008, which perform well across the L/T transition (T. J. Dupuy et al. 2015; T. J. Dupuy & M. C. Liu 2017; M. Chen et al. 2022).

4.2. *Goodness-of-fit test for mass, age, and luminosity*

In the three-dimensional parameter space defined by mass, age, and luminosity, the evolutionary models form two-dimensional manifolds, whereas the observations correspond to a single point with associated uncertainties. We assess the goodness of fit by evaluating how close the observed point lies to each model manifold. To quantify this, we compute the Mahalanobis distance D^2, which reduces to a χ^2 metric in the absence of correlations among variables, which is a reasonable assumption in our case. The observed luminosity and dynamical mass both depend on the measured parallax to the host star, but its uncertainty is an irrelevantly small contribution to the total uncertainties for these two quantities. The asteroseismic analysis also did not use the parallax.

We determined the distance D^2 between the observed point and the nearest point on each model manifold. The distance

D^2 follows a chi-squared distribution with 1 degree of freedom, corresponding to the single direction normal to the two-dimensional manifold in three-dimensional parameter space (3–2). We calculated the one-sided tail probability p, defined as the probability that a random draw from this distribution exceeds the observed D^2. The probability p is then converted to an equivalent σ value using the inverse survival function of a normal distribution. The results are reported in Table 6.

We see that the overall trends are consistent with those from the tests performed earlier, with CBPD2023 showing the best agreement with the observations. The σ values reported are also generally lower than those reported from the consistency tests because the current method allows the model to move along the manifold surface to find the closest point to the observations. This always yields the smallest possible residual compatible with the model. In contrast, the consistency test fixes two coordinates at their observed values and evaluates the residual in the third dimension. It does not allow movement along the surface, so the resulting residual is measured along a coordinate direction rather than normal to the surface, and is therefore typically larger.

5. NEAR-SIMULTANEOUS ASTEROSEISMOLOGY WITH TESS

TESS observed HR 7672 in Sectors 54 and 81 with a 20-second cadence exposure. We analysed the SPOC light curves to search for oscillation signals in the TESS data. Figure 10(a) shows the Pre-search Data Conditioning SAP (PDCSAP) flux, which removes long-term trends from instrumental drifts as well as rotational modulation. The timestamps indicate that our KPF monitoring campaign began exactly three days before the start of Sector 81, yielding nearly contemporaneous RV and photometric coverage. Figure 10(b) displays the corresponding power spectrum of the TESS time series, with vertical lines marking the oscillation frequencies extracted from the KPF RVs. The oscillation signature is detectable but very weak. This is confirmed in Figure 11: the ridges corresponding to the same ℓ-degrees are only marginally discernible in both the échelle diagram and the collapsed échelle diagram.

To confirm these are real oscillation signals, we cross-correlated the TESS power spectrum with a template constructed from the KPF frequencies. This method of cross correlation should be more sensitive to regular structures in the spectrum. For each mode frequency listed in Table 1 (before applying the line-of-sight correction), we generated a unit-height, unit-width Lorentzian profile centered on that frequency and summed all these profiles to form the template. Figure 12 presents the cross-correlation coefficient as a function of lag between the template and TESS power spectra. The pronounced peak at zero lag confirms that the oscillation signals are indeed present in the TESS data. Additional peaks at integer multiples of $\Delta\nu$ and at linear combinations of $\Delta\nu$ and $\delta\nu_{0,l}$ further confirm the underlying comb structure. For comparison, we also include the cross-correlation spectrum between the template and a noise spectrum generated from normally distributed white noise with typical RV uncertainties. This noise cross-correlation shows no significant features.

Because oscillation frequencies are detected in both the TESS and KPF datasets, HR 7672 offers an opportunity to constrain photometry-to-RV amplitude ratios. These ratios have previously been measured in only a few stars with simultaneous data, including Procyon (D. Huber et al. 2011b), HD 35833 (A. F. Gupta et al. 2022), and β Aql (H. Kjeldsen et al. 2025). We follow the approach of H. Kjeldsen et al. (2008) to measure oscillation amplitudes. Each power density spectrum — defined as the power spectrum multiplied by the effective observing duration — was smoothed with a Gaussian kernel with a full width at half-maximum of $4\Delta\nu$ to produce a single power excess hump. The smoothed spectrum was then multiplied by $\Delta\nu/c$ to estimate the power per radial order, where c accounts for the effective number of modes per order (J. Ballot et al. 2011). Given the star's similarity to the Sun, we adopt solar values calculated by H. Kjeldsen et al. (2008): $c = 4.09$ for velocity data and $c = 2.91$ for TESS photometry. Figure 13 shows the resulting spectra. The square root of the maximum near $\nu_{\max}$ yields the oscillation amplitude. Uncertainties in the oscillation amplitudes were estimated via bootstrapping: in each realization, the original spectrum was multiplied by a noise spectrum, and the oscillation amplitude was remeasured. The spread in amplitude estimates across all realizations was adopted as the uncertainty.

For the KPF data, we measured a RV amplitude of 17.1 ± 0.7 cm s^{-1}. In the TESS data, oscillations are not clearly visible as a distinct power excess due to dominant contributions from granulation and white noise. We therefore derive an upper limit of 2.9 ± 0.7 ppm for the photometric amplitude in the TESS bandpass. Applying a bolometric correction factor of 1.2 (M. N. Lund 2019), the corresponding bolometric amplitude is 3.48 ± 0.84 ppm. These values yield an upper limit on the bolometric photometry-to-RV amplitude ratio of 20.1 ± 7.6 ppm (m s^{-1})$^{-1}$. Both the amplitudes and their ratio are similar to the solar values. For comparison, the solar oscillation amplitude is approximately 18.7 cm s^{-1} in RV (H. Kjeldsen et al. 2008) and 3.6 ppm in photometry (E. Michel et al. 2009), corresponding to a ratio of about 19.2 ppm (m s^{-1})$^{-1}$.

Further, both the amplitudes and their ratio are broadly in line with predictions from 3D hydrodynamic simulations (Y. Zhou et al. 2021). Repeating the methods of Y. Zhou et al. (2021), we obtained a simulated solar amplitude ratio between bolometric intensity and fluid velocity of 20.12 ppm (m s^{-1})$^{-1}$. For a hotter main-sequence model whose basic stellar parameters are close to those of HR 7672A ($T_{\rm eff}$ = 6000 K and $\log g$ = 4.5 dex), the amplitude ratio is slightly lower at 19.27 ppm (m s^{-1})$^{-1}$. The trend predicted from simulations is also consistent with the empirical amplitude scaling relation of H. Kjeldsen & T. R. Bedding (1995). Assuming the conversion factor between fluid velocity and RV is invariant from the Sun to HR 7672A, which is reasonable given the similarity between the two stars, the expectation is that the actual photometry-to-RV amplitude ratio

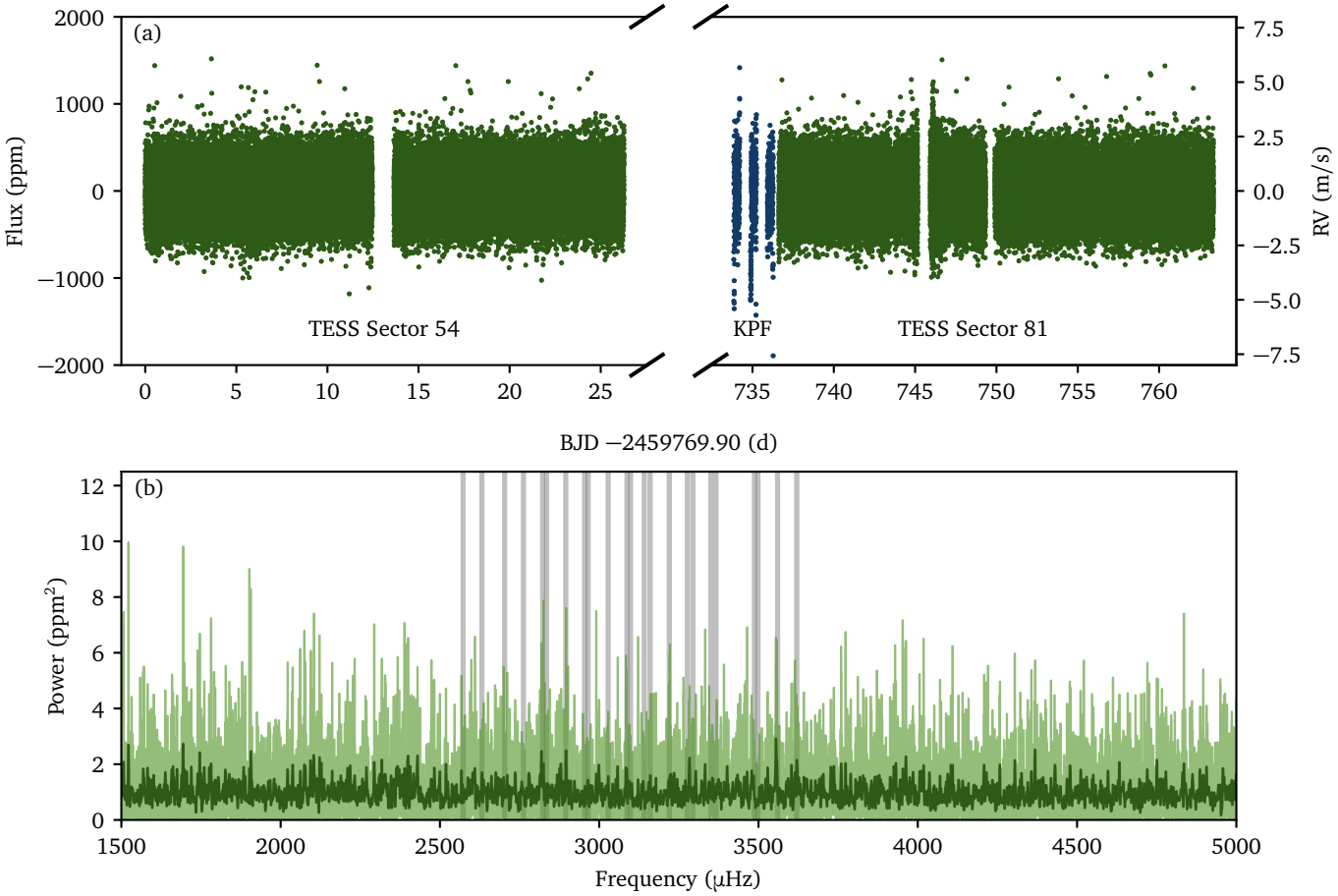

Figure 10. (a): TESS photometric observations of HR 7672 from Sectors 54 and 81. The KPF data were collected three days prior to the start of TESS Sector 81, resulting near-simultaneous coverage. (b): Power spectrum of the TESS light curve. The vertical lines highlight the oscillation frequencies derived from the KPF radial velocity data (Table 1).

of the latter is slightly smaller than 19.2 ppm $(\mathrm{m\ s^{-1}})^{-1}$, in agreement with our measured upper limit.

Oscillation amplitudes are expected to be lower in stars with higher magnetic activity (T. L. Campante et al. 2014; M. Sayeed et al. 2025). M. Sayeed et al. (2025) quantified this dependency using the chromospheric activity levels derived from Ca II H&K line emission, using the logarithmic flux ratio between the emission flux and the bolometric flux, $\log R'_{\mathrm{HK}}$. S. Boro Saikia et al. (2018) reported $\log R'_{\mathrm{HK}}$ values between −4.68 and −4.74 for this star; for comparison, the solar value is around −4.94 (R. Egeland et al. 2017). According to Equation 10 of M. Sayeed et al. (2025), this corresponds to an amplitude ratio between 0.81 and 0.85 relative to the Sun. Although our measurement is broadly consistent with this prediction, it does not provide conclusive evidence for a reduced amplitude in this star due to the large uncertainties. The photometric-to-RV amplitude ratio, however, is likely less affected by magnetic activities, as it depends on the stellar structure near the photosphere to a first order (Y. Zhou et al. 2021). By comparing hydrodynamics and magnetohydrodynamics simulations of stellar atmospheres, T. S. Bhatia et al. (2022) show that changes in near-surface density, temperature, and pressure stratification caused by the small-scale dynamo are less than 1% for G-type stars.

6. CONCLUSIONS

In this work, we obtained three nights of extremely precise RV data for HR 7672A with the Keck Planet Finder and determined the stellar age using RV asteroseismology and activity-based gyrochronology. We also obtained a new epoch of astrometry for HR 7672B and, combined with new long-term RV monitoring of the host star, resulted in a more precise dynamical mass for the system. The resulting measurements enable a direct high-precision test of brown dwarf evolutionary models at the stellar/substellar boundary. Our main findings are as follows:

1. Asteroseismic modeling of HR 7672A yields an age of 1.87 ± 0.65 Gyr; gyrochronology gives 2.39 ± 0.48 Gyr; and a joint analysis provides a final estimate of 2.26 ± 0.40 Gyr, corresponding to a 18% fractional uncertainty for this young Sun-like star.

2. Modeling of the relative astrometry, RV, and Hipparcos-Gaia accelerations data produced the the

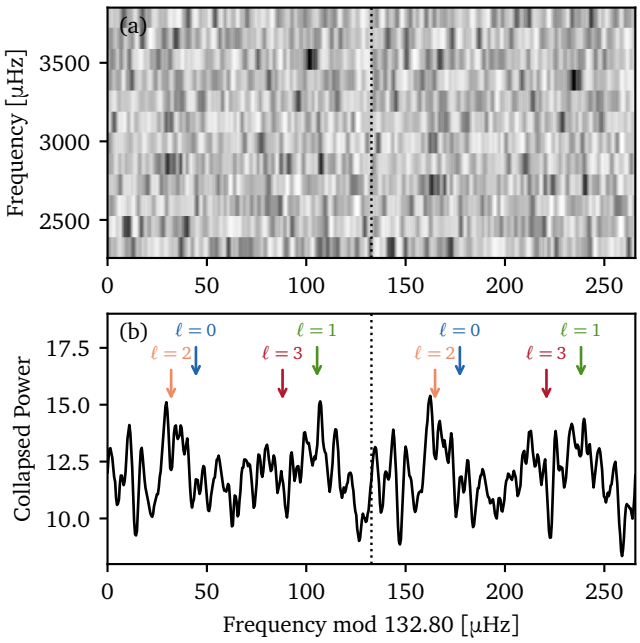

Figure 11. (a): Replicated échelle diagram of the TESS power spectrum. (b): Collapsed échelle diagram, by summing the power along the y-axis of panel (a). The expected mode positions, informed by the KPF data, are indicated by arrows.

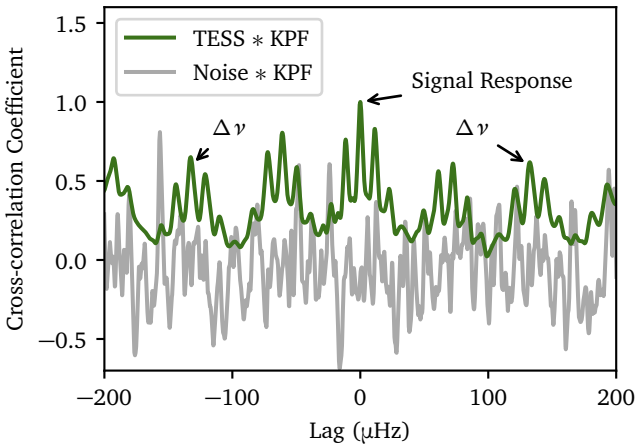

Figure 12. Cross-correlation coefficient between a template power spectrum, constructed using frequencies extracted from KPF RV data, and the TESS power spectrum. For comparison, the cross–correlation coefficient between the same template spectrum and a noise power spectrum generated from a random draw is also shown.

dynamical orbit of the system, resulting in revised dynamical masses of 1.111 ± 0.017 $M_\odot$ for HR 7672A and 75.39 ± 0.67 M_{Jup} for HR 7672B.

3. We performed consistency tests on six sets of brown dwarf evolutionary models against the observed mass, age, and luminosity of the companion. Each test used two of these quantities as inputs and compared the model predictions for the third. The CBPD2023 models (G. Chabrier et al. 2023), which incorporates an updated equation of state, showing excellent agreement, within $< 0.3\sigma$ of all the observations. The other 5 sets of models agree within 1–3σ of the observations depending on the test. Also, three of them (Diamondback, SM2008, and BHAC2015) struggle to predict luminosities as low as the observed luminosity, a discrepancy that is independent of the system's age (Figure 8).

4. We also conducted goodness-of-fit tests by measuring the distance of the observed properties from the two-dimensional manifold defined by each evolutionary model in the three-dimensional (mass, age, luminosity) space. The CBPD2023 models again show the best overall agreement, while the other models are consistent within 1–2σ.

5. TESS observed the system nearly simultaneously with our KPF monitoring. We detected a weak seismic signal in the TESS data and constrained the photometry-to-RV oscillation amplitude ratio to be close to the solar value, consistent with predictions from 3D hydrodynamical simulations.

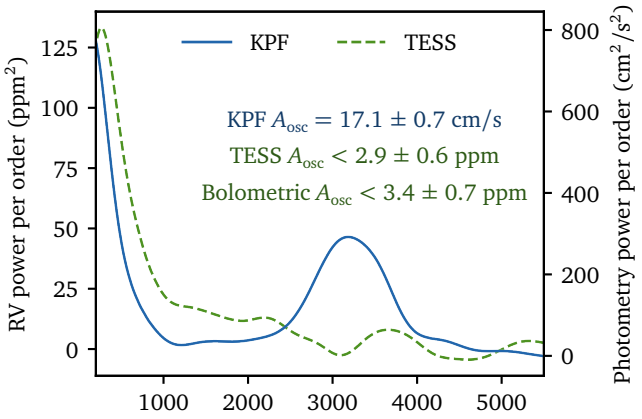

Figure 13. Power per radial order spectra computed from both KPF RV data and TESS photometric data.

Future measurements of HR 7672B's bolometric luminosity, for example with JWST photometry, could significantly improve its precision. Combined with a more precise astrometric solution from Gaia DR4, which will benefit from a baseline roughly twice long as Gaia DR3, the dynamical mass constraints are expected to improve further. As shown in Figure 7, these improvements could enable much stronger discrimination among cooling models. This is especially valuable for testing their performance near the stellar/substellar boundary, where HR 7672B resides. Some evolutionary models already predict that hydrogen fusion may occur in the future of this object. With these new measurements, HR 7672B will continue to serve as one of the most robust benchmarks for brown dwarf evolution and cooling

physics. Moreover, the differences between models in this mass range increases for older ages, so the discovery of older analogs to the HR 7672AB system from, e.g., Gaia DR4, will be exceptionally valuable to test our understanding of the evolution of low-mass stars and brown dwarfs.

ACKNOWLEDGEMENTS

The authors wish to recognize and acknowledge the very significant cultural role and reverence that the summit of Maunakea has always had within the Native Hawaiian community. We are most fortunate to have the opportunity to conduct observations from this mountain. Y.L. acknowledges support from the National Aeronautics and Space Administration (80NSSC25K7904) and the Beatrice Watson Parrent Fellowship. M.L. acknowledges past support from the Parrent Fellowship 24 years ago that enabled the discovery of HR 7672B and current support from the the Gordon and Betty Moore Foundation through grant GBMF8550. T.S.M. acknowledges support from NASA grant 80NSSC25K7898. T.R.B. acknowledges support from the Australian Research Council (FL220100117). T.L.C. is supported by Fundação para a Ciência e a Tecnologia (FCT) in the form of a work contract (2023.08117.CEECIND/CP2839/CT0004). J.R.L. and M.S.L. acknowledge support from VILLUM FONDEN (42101) and The Independent Research Fund Denmark's Inge Lehmann program (1131-00014B).

REFERENCES

Adelberger, E. G., Austin, S. M., Bahcall, J. N., et al. 1998, Reviews of Modern Physics, 70, 1265

An, Q., Brandt, T. D., Brandt, G. M., & Venner, A. 2025, ApJS, 280, 61

Angulo, C., Arnould, M., Rayet, M., et al. 1999, NuPhA, 656, 3

Antia, H. M., & Basu, S. 1994, A&AS, 107, 421

Asplund, M., Grevesse, N., Sauval, A. J., & Scott, P. 2009, ARA&A, 47, 481

Bahcall, J. N., Pinsonneault, M. H., & Wasserburg, G. J. 1995, Reviews of Modern Physics, 67, 781

Bailer-Jones, C. A. L., Rybizki, J., Fouesneau, M., Demleitner, M., & Andrae, R. 2021, AJ, 161, 147

Ball, W. H., & Gizon, L. 2014, A&A, 568, A123

Ballot, J., Barban, C., & van't Veer-Menneret, C. 2011, A&A, 531, A124

Baraffe, I., Chabrier, G., Allard, F., & Hauschildt, P. H. 2002, A&A, 382, 563

Baraffe, I., Homeier, D., Allard, F., & Chabrier, G. 2015, A&A, 577, A42

Barnes, S. A., Weingrill, J., Fritzewski, D., Strassmeier, K. G., & Platais, I. 2016, ApJ, 823, 16

Bellinger, E. P. 2019, MNRAS, 486, 4612

Berger, T. A., Huber, D., van Saders, J. L., et al. 2020, AJ, 159, 280

Best, W. M. J., Magnier, E. A., Liu, M. C., et al. 2018, ApJS, 234, 1

Bhatia, T. S., Cameron, R. H., Solanki, S. K., et al. 2022, A&A, 663, A166

Boccaletti, A., Chauvin, G., Lagrange, A. M., & Marchis, F. 2003, A&A, 410, 283

Böhm-Vitense, E. 1958, ZA, 46, 108

Boro Saikia, S., Marvin, C. J., Jeffers, S. V., et al. 2018, A&A, 616, A108

Bouma, L. G., Hillenbrand, L. A., Howard, A. W., et al. 2024, ApJ, 976, 234

Bowler, B. P., Tran, Q. H., Zhang, Z., et al. 2023, AJ, 165, 164

Brandt, G. M., Dupuy, T. J., Li, Y., et al. 2021, AJ, 162, 301

Brandt, T. D., Dupuy, T. J., & Bowler, B. P. 2019, AJ, 158, 140

Brandt, T. D., Dupuy, T. J., Li, Y., et al. 2021, orvara: Orbits from Radial Velocity, Absolute, and/or Relative Astrometry. http://ascl.net/2105.012

Burrows, A., Marley, M., Hubbard, W. B., et al. 1997, ApJ, 491, 856

Campante, T. L., Chaplin, W. J., Lund, M. N., et al. 2014, ApJ, 783, 123

Campante, T. L., Kjeldsen, H., Li, Y., et al. 2024, A&A, 683, L16

Castelli, F., & Kurucz, R. L. 2003, in IAU Symposium, Vol. 210, Modelling of Stellar Atmospheres, ed. N. Piskunov, W. W. Weiss, & D. F. Gray, A20

Chabrier, G., & Baraffe, I. 1997, A&A, 327, 1039

—. 2000, ARA&A, 38, 337

Chabrier, G., Baraffe, I., Phillips, M., & Debras, F. 2023, A&A, 671, A119

Chen, M., Li, Y., Brandt, T. D., et al. 2022, AJ, 163, 288

Chiti, F., van Saders, J. L., Heintz, T. M., et al. 2024, arXiv e-prints, arXiv:2403.12129

Christensen-Dalsgaard, J. 1984, in Space Research in Stellar Activity and Variability, ed. A. Mangeney & F. Praderie, 11

Christensen-Dalsgaard, J. 2008a, Ap&SS, 316, 13

—. 2008b, Ap&SS, 316, 113

Cox, J. P., & Giuli, R. T. 1968, Principles of stellar structure

Crepp, J. R., Johnson, J. A., Fischer, D. A., et al. 2012, ApJ, 751, 97

Curtis, J. L., Agüeros, M. A., Douglas, S. T., & Meibom, S. 2019, ApJ, 879, 49

Curtis, J. L., Agüeros, M. A., Matt, S. P., et al. 2020, ApJ, 904, 140

Cutri, R. M., Skrutskie, M. F., van Dyk, S., et al. 2003, 2MASS All Sky Catalog of point sources.

Cyburt, R. H., Amthor, A. M., Ferguson, R., et al. 2010, ApJS, 189, 240

Davies, G. R., Handberg, R., Miglio, A., et al. 2014, MNRAS, 445, L94

Demarque, P., Guenther, D. B., Li, L. H., Mazumdar, A., & Straka, C. W. 2008, Ap&SS, 316, 31

Donahue, R. A., Saar, S. H., & Baliunas, S. L. 1996, ApJ, 466, 384

Douglas, S. T., Agüeros, M. A., Covey, K. R., & Kraus, A. 2017, ApJ, 842, 83

Douglas, S. T., Curtis, J. L., Agüeros, M. A., et al. 2019, ApJ, 879, 100

Dungee, R., van Saders, J., Gaidos, E., et al. 2022, ApJ, 938, 118

Dupuy, T. J., Kratter, K. M., Kraus, A. L., et al. 2016, ApJ, 817, 80

Dupuy, T. J., & Liu, M. C. 2017, ApJS, 231, 15

Dupuy, T. J., Liu, M. C., Evans, E. L., et al. 2023, MNRAS, 519, 1688

Dupuy, T. J., Liu, M. C., & Ireland, M. J. 2009, ApJ, 692, 729

Dupuy, T. J., Liu, M. C., Leggett, S. K., et al. 2015, ApJ, 805, 56

Eddington, A. S. 1926, The Internal Constitution of the Stars

Egeland, R., Soon, W., Baliunas, S., et al. 2017, ApJ, 835, 25

Epstein, C. R., & Pinsonneault, M. H. 2014, ApJ, 780, 159

ESA, ed. 1997, ESA Special Publication, Vol. 1200, The HIPPARCOS and TYCHO catalogues. Astrometric and photometric star catalogues derived from the ESA HIPPARCOS Space Astrometry Mission

Feng, F., Butler, R. P., Jones, H. R. A., et al. 2021, MNRAS, 507, 2856

Fischer, D. A., Marcy, G. W., & Spronck, J. F. P. 2014, ApJS, 210, 5

Fischer, D. A., Anglada-Escude, G., Arriagada, P., et al. 2016, PASP, 128, 066001

Foreman-Mackey, D. 2018, Research Notes of the American Astronomical Society, 2, 31

Formicola, A., Imbriani, G., Costantini, H., et al. 2004, Physics Letters B, 591, 61

Frandsen, S., Jones, A., Kjeldsen, H., et al. 1995, A&A, 301, 123

Gaia Collaboration. 2022, VizieR Online Data Catalog: Gaia DR3 Part 1. Main source (Gaia Collaboration, 2022), VizieR On-line Data Catalog: I/355. Originally published in: doi:10.1051/0004-63, doi: 10.26093/cds/vizier.1355

Gibson, S. R. 2016, in Society of Photo-Optical Instrumentation Engineers (SPIE) Conference Series, Vol. 9911, Modeling, Systems Engineering, and Project Management for Astronomy VI, ed. G. Z. Angeli & P. Dierickx, 99112C

Gibson, S. R., Howard, A. W., Roy, A., et al. 2018, in Society of Photo-Optical Instrumentation Engineers (SPIE) Conference Series, Vol. 10702, Ground-based and Airborne Instrumentation for Astronomy VII, ed. C. J. Evans, L. Simard, & H. Takami, 107025X

Gibson, S. R., Howard, A. W., Rider, K., et al. 2020, in Society of Photo-Optical Instrumentation Engineers (SPIE) Conference Series, Vol. 11447, Ground-based and Airborne Instrumentation for Astronomy VIII, ed. C. J. Evans, J. J. Bryant, & K. Motohara, 1144742

Gibson, S. R., Howard, A. W., Rider, K., et al. 2024, in Society of Photo-Optical Instrumentation Engineers (SPIE) Conference Series, Vol. 13096, Ground-based and Airborne Instrumentation for Astronomy X, ed. J. J. Bryant, K. Motohara, & J. R. D. Vernet, 1309609

Gold, R. 1964,

Grevesse, N., & Sauval, A. J. 1998, SSRv, 85, 161

Gupta, A. F., Luhn, J., Wright, J. T., et al. 2022, AJ, 164, 254

Hall, O. J., Davies, G. R., van Saders, J., et al. 2021, Nature Astronomy, 5, 707

Hammer, J. W., Fey, M., Kunz, R., et al. 2005, NuPhA, 758, 363

Hauschildt, P. H., Allard, F., & Baron, E. 1999a, ApJ, 512, 377

Hauschildt, P. H., Allard, F., Ferguson, J., Baron, E., & Alexander, D. R. 1999b, ApJ, 525, 871

Henyey, L., Vardya, M. S., & Bodenheimer, P. 1965, ApJ, 142, 841

Herwig, F. 2000, A&A, 360, 952

Hon, M., Li, Y., & Ong, J. 2024a, ApJ, 973, 154

Hon, M., Huber, D., Li, Y., et al. 2024b, arXiv e-prints, arXiv:2407.21234

Huber, D., Bedding, T. R., Stello, D., et al. 2011a, ApJ, 743, 143

Huber, D., Bedding, T. R., Arentoft, T., et al. 2011b, ApJ, 731, 94

Huber, D., Zinn, J., Bojsen-Hansen, M., et al. 2017, ApJ, 844, 102

Jermyn, A. S., Bauer, E. B., Schwab, J., et al. 2023, ApJS, 265, 15

Kasagi, Y., Kawashima, Y., Kawahara, H., et al. 2025, arXiv e-prints, arXiv:2508.01281

Kjeldsen, H., & Bedding, T. R. 1995, A&A, 293, 87

Kjeldsen, H., Bedding, T. R., Arentoft, T., et al. 2008, ApJ, 682, 1370

Kjeldsen, H., Bedding, T. R., Li, Y., et al. 2025, arXiv e-prints, arXiv:2506.00493

Krishna Swamy, K. S. 1966, ApJ, 145, 174

Li, Y., Bedding, T. R., Stello, D., et al. 2023, MNRAS, 523, 916

Li, Y., Huber, D., Ong, J. M. J., et al. 2025, ApJ, 984, 125

Liu, M. C., Dupuy, T. J., & Ireland, M. J. 2008, ApJ, 689, 436

Liu, M. C., Fischer, D. A., Graham, J. R., et al. 2002, ApJ, 571, 519

Lomb, N. R. 1976, Ap&SS, 39, 447

Long, L., Bi, S., Zhang, J., et al. 2023, ApJS, 268, 30

Lu, Y., Angus, R., Foreman-Mackey, D., & Hattori, S. 2024, AJ, 167, 159

Lund, M. N. 2019, MNRAS, 489, 1072

Lundkvist, M. S., Kjeldsen, H., Bedding, T. R., et al. 2024, ApJ, 964, 110

Mamajek, E. E., & Hillenbrand, L. A. 2008, ApJ, 687, 1264

Marley, M. S., Fortney, J. J., Hubickyj, O., Bodenheimer, P., & Lissauer, J. J. 2007, ApJ, 655, 541

Marley, M. S., Saumon, D., Visscher, C., et al. 2021, ApJ, 920, 85

Meibom, S., Barnes, S. A., Platais, I., et al. 2015, Nature, 517, 589

Messina, S., Rodonò, M., & Guinan, E. F. 2001, A&A, 366, 215

Michaud, G., & Proffitt, C. R. 1993, in Astronomical Society of the Pacific Conference Series, Vol. 40, IAU Colloq. 137: Inside the Stars, ed. W. W. Weiss & A. Baglin, 246–259

Michel, E., Samadi, R., Baudin, F., et al. 2009, A&A, 495, 979

Moedas, N., Bossini, D., Deal, M., & Cunha, M. S. 2024, A&A, 684, A113

Morháč, M., Matoušek, V., & Kliman, J. 2003, Digital Signal Processing, 13, 144

Morley, C. V., Fortney, J. J., Marley, M. S., et al. 2012, ApJ, 756, 172

Morley, C. V., Mukherjee, S., Marley, M. S., et al. 2024, ApJ, 975, 59

Ong, J. M. J., Basu, S., & McKeever, J. M. 2021, ApJ, 906, 54

Paxton, B., Bildsten, L., Dotter, A., et al. 2011, ApJS, 192, 3

Paxton, B., Cantiello, M., Arras, P., et al. 2013, ApJS, 208, 4

Paxton, B., Marchant, P., Schwab, J., et al. 2015, ApJS, 220, 15

Paxton, B., Schwab, J., Bauer, E. B., et al. 2018, ApJS, 234, 34

Paxton, B., Smolec, R., Schwab, J., et al. 2019, ApJS, 243, 10

Phillips, M. W., Tremblin, P., Baraffe, I., et al. 2020a, aap, 637, A38

—. 2020b, A&A, 637, A38

Pinfield, D. J., Jones, H. R. A., Lucas, P. W., et al. 2006, MNRAS, 368, 1281

Radick, R., & Pevtsov, A. 2018, HK_Project_v1995_NSO, Harvard Dataverse dataset, doi: 10.7910/DVN/ZRJ6NT

Rebull, L. M., Stauffer, J. R., Bouvier, J., et al. 2016, AJ, 152, 113

Ricker, G. R., Winn, J. N., Vanderspek, R., et al. 2015, Journal of Astronomical Telescopes, Instruments, and Systems, 1, 014003

Riello, M., De Angeli, F., Evans, D. W., et al. 2021, A&A, 649, A3

Rosenthal, L. J., Fulton, B. J., Hirsch, L. A., et al. 2021, ApJS, 255, 8

Roxburgh, I. W. 2016, A&A, 585, A63

Roxburgh, I. W., & Vorontsov, S. V. 1994, MNRAS, 268, 143

—. 2003, A&A, 411, 215

Saumon, D., & Marley, M. S. 2008, ApJ, 689, 1327

Saumon, D., Marley, M. S., Cushing, M. C., et al. 2006, ApJ, 647, 552

Saunders, N., van Saders, J. L., Lyttle, A. J., et al. 2024, ApJ, 962, 138

Sayeed, M., Huber, D., Chontos, A., & Li, Y. 2025, arXiv e-prints, arXiv:2503.15599

Scargle, J. D. 1982, ApJ, 263, 835

Scherrer, P. H., Wilcox, J. M., Christensen-Dalsgaard, J., & Gough, D. O. 1983, SoPh, 82, 75

Serabyn, E., Mawet, D., Bloemhof, E., et al. 2009, ApJ, 696, 40

Serenelli, A., Johnson, J., Huber, D., et al. 2017, ApJS, 233, 23

Service, M., Lu, J. R., Campbell, R., et al. 2016, PASP, 128, 095004

Silva Aguirre, V., Davies, G. R., Basu, S., et al. 2015, MNRAS, 452, 2127

Silva Aguirre, V., Lund, M. N., Antia, H. M., et al. 2017, ApJ, 835, 173

Somers, G., Stauffer, J., Rebull, L., Cody, A. M., & Pinsonneault, M. 2017, ApJ, 850, 134

Sonoi, T., Samadi, R., Belkacem, K., et al. 2015, A&A, 583, A112

Spada, F., & Lanzafame, A. C. 2020, A&A, 636, A76

Tassoul, M. 1980, ApJS, 43, 469

—. 1990, ApJ, 358, 313

Tayar, J., Claytor, Z. R., Huber, D., & van Saders, J. 2022, ApJ, 927, 31

Thoul, A. A., Bahcall, J. N., & Loeb, A. 1994, ApJ, 421, 828

Tokunaga, A. T., Simons, D. A., & Vacca, W. D. 2002, PASP, 114, 180

Townsend, R. H. D., & Teitler, S. A. 2013, MNRAS, 435, 3406

Trampedach, R., Stein, R. F., Christensen-Dalsgaard, J., Nordlund, Å., & Asplund, M. 2014, MNRAS, 445, 4366

Tremblin, P., Amundsen, D. S., Mourier, P., et al. 2015, ApJL, 804, L17

Ulrich, R. K. 1986, ApJL, 306, L37

van Saders, J. L., Ceillier, T., Metcalfe, T. S., et al. 2016, Nature, 529, 181

van Saders, J. L., & Pinsonneault, M. H. 2013, ApJ, 776, 67

Wang, J., Kolecki, J. R., Ruffio, J.-B., et al. 2022, AJ, 163, 189

Weiss, A., & Schlattl, H. 2008, Ap&SS, 316, 99

White, T. R., Bedding, T. R., Stello, D., et al. 2011, ApJ, 743, 161

White, T. R., Bedding, T. R., Gruberbauer, M., et al. 2012, ApJL, 751, L36

Wright, J. T. 2018, in Handbook of Exoplanets, ed. H. J. Deeg & J. A. Belmonte, 4

Zhang, J., Huber, D., Weiss, L. M., et al. 2024, AJ, 168, 295

Zhou, Y., Nordlander, T., Casagrande, L., et al. 2021, MNRAS, 503, 13

Table 7. Long-baseline radial-velocity data of HR 7672A.

BJD	RV	σ(RV)	Instrument
d	km s^{-1}	km s^{-1}	
2447047.72690000	0.2516200	0.0089100	Lick Observatory (Fischer)
2447373.79930000	0.2209600	0.0101700	Lick Observatory (Fischer)
2447373.80310000	0.2141700	0.0100600	Lick Observatory (Fischer)
2447373.80690000	0.2179700	0.0100500	Lick Observatory (Fischer)
2447373.81110000	0.2180600	0.0100500	Lick Observatory (Fischer)
2447373.81500000	0.1992400	0.0092300	Lick Observatory (Fischer)
2447373.81900000	0.2152500	0.0116400	Lick Observatory (Fischer)
2447373.93090000	0.2061600	0.0102500	Lick Observatory (Fischer)
2447373.93700000	0.2005600	0.0102500	Lick Observatory (Fischer)
2447374.83330000	0.1660100	0.0131700	Lick Observatory (Fischer)
...	...	...	...

NOTE—Only the first 10 lines are shown. The full table can be accessed online.

APPENDIX

A. HIGH-CADENCE RADIAL VELOCITY DATA

Table 7 presents the long-baseline radial velocity measurements. Combined with the astrometric data, these are used to model the dynamical orbit of the HR 7672AB. Table 8 lists the high-cadence radial velocity measurements obtained over three consecutive nights with the Keck Planet Finder. These data are used to extract the stellar oscillation frequencies for HR 7672A.

B. DYNAMICAL ORBIT FIT

Figures 14 and 15 present the best-fitting dynamical orbit model to the astrometric and long-baseline radial velocity data. The corresponding parameter estimates are listed in Table 9.

Table 8. High-cadence radial-velocity data of HR 7672A measured from KPF spectra over three consecutive nights.

BJD	RV	σ(RV)
d	km s^{-1}	km s^{-1}
2460503.80257248	5.6694026	0.0025670
2460503.80334406	5.6723237	0.0024898
2460503.80402596	5.6720894	0.0023852
2460503.80475537	5.6711032	0.0035657
2460503.80531227	5.6676321	0.0029298
2460503.80612872	5.6679721	0.0030534
2460503.80752271	5.6661874	0.0033515
2460503.80882304	5.6660599	0.0050862
...	...	...

Note—Only the first 10 lines are shown. The full table can be accessed online.

Table 9. Orbital parameters estimated for HR 7672AB

Parameter	Prior	Median $\pm1\sigma$
Stellar parameters		
Host-star mass M_A ($M_\odot$)	-	$1.111^{+0.017}_{-0.017}$
Companion mass M_B (M_{Jup})	-	$75.39^{+0.67}_{-0.67}$
Orbital parameters		
Semi-major axis a_B (AU)	-	$16.88^{+0.10}_{-0.10}$
Orbital period P_B (yr)	-	$63.77^{+0.63}_{-0.61}$
Inclination i_B (deg)	-	$97.73^{+0.31}_{-0.31}$
$\sqrt{e_B}\sin\omega_B$	-	$-0.6828^{+0.0021}_{-0.0021}$
$\sqrt{e_B}\cos\omega_B$	-	$-0.0450^{+0.0054}_{-0.0055}$
Eccentricity e_B	$\mathcal{U}(0, 0.99)$	$0.4683^{+0.0032}_{-0.0031}$
Mean longitude at t_{ref} = 2455197.5 JD, λ_{ref} (deg)	-	$237.29^{+0.18}_{-0.18}$
Longitide of the ascending node Ω_B (deg)	-	$330.88^{+0.21}_{-0.21}$
Parallax (mas)	$\mathcal{N}(\varpi_{DR3}, \sigma[\varpi_{DR3}])^*$	$56.2724^{+0.0094}_{-0.0094}$
Argument of periastron ω_B (deg)	-	$266.23^{+0.45}_{-0.45}$
Time of periastron $T_0 = t_{ref} - P\frac{\lambda-\omega}{360}$ (JD)	-	2457070^{+11}_{-11}
Other Parameters		
Lick Fischer RV zero point (m s^{-1})	-	$-307.8^{+2.4}_{-2.4}$
HIRES pre RV zero point (m s^{-1})	-	$-417.1^{+2.2}_{-2.2}$
HIRES post RV zero point (m s^{-1})	-	$-414.4^{+2.4}_{-2.3}$
APF RV zero point (m s^{-1})	-	$14.6^{+2.2}_{-2.2}$

Note—* ϖ_{DR3} and $\sigma[\varpi_{DR3}]$ present the parallax and parallax uncertainty of HR7672 from Gaia DR3 observations.

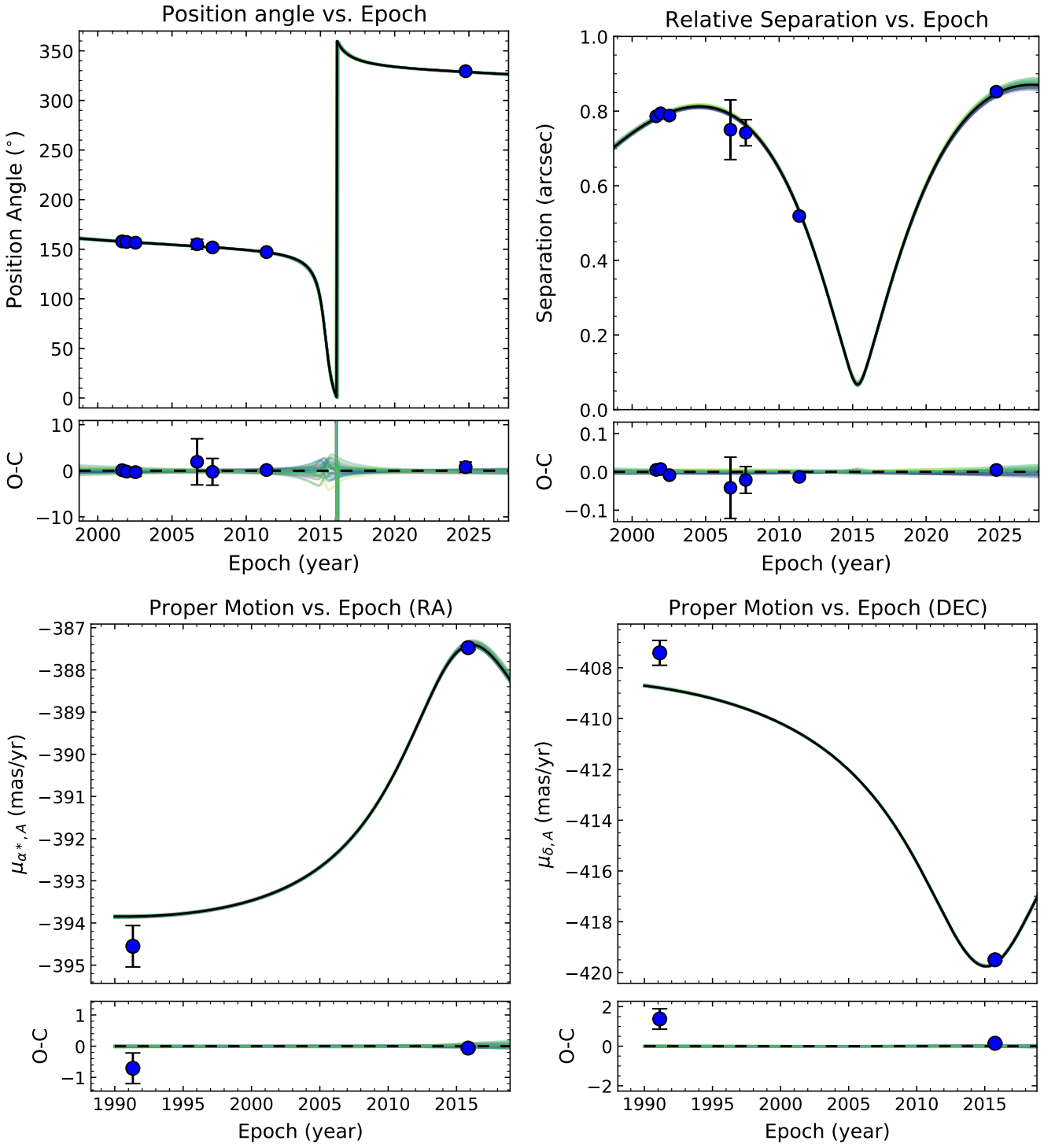

Figure 14. Relative and absolute astrometry measurements of the HR 7672 system, fitted with a dynamical model jointly constrained by the long-baseline radial velocities. Residuals relative to the best-fit model are also shown.

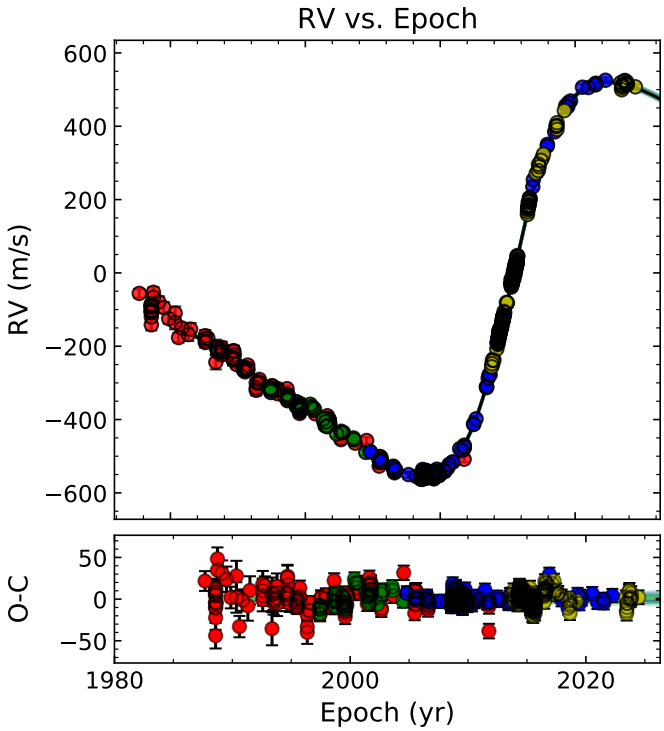

Figure 15. Top: Long-baseline radial velocity measurements of HR 7672 A, fitted with a dynamical model jointly constrained by astrometric data. Colored symbols indicate radial velocities measured by different instruments: Lick-Fischer, HIRES (pre and post upgrade), and APF. Bottom: residuals relative to the best-fit model.